An overview of sea state conditions and air-sea fluxes during RaDyO

Christopher J. Zappa,[1] Michael L. Banner,[2] Howard Schultz,[3] Johannes R. Gemmrich,[4] Russel P. Morison,[5] Deborah A. LeBel,[1] and Tommy Dickey[6]

[1]   Refining radiative-transfer modeling capabilities for light transmission through the sea surface requires a more detailed prescription of the sea surface roughness beyond the probability density function of the sea surface slope field. To meet this need, exciting new measurement methodologies now provide the opportunity to enhance present knowledge of sea surface roughness, especially at the microscale. In this context, two intensive field experiments using R/P *Floating Instrument Platform* were staged within the Office of Naval Research's Radiance in a Dynamic Ocean (RaDyO) field program in the Santa Barbara Channel and in the central Pacific Ocean south of Hawaii. As part of this program, our team gathered and analyzed a comprehensive suite of sea surface roughness measurements designed to provide optimal coverage of fundamental optical distortion processes associated with the air-sea interface. This contribution describes the ensemble of instrumentation deployed. It provides a detailed documentation of the ambient environmental conditions that prevailed during the RaDyO field experiments. It also highlights exciting new sea surface roughness measurement capabilities that underpin a number of the scientific advances resulting from the RaDyO program. For instance, a new polarimetric imaging camera highlights the complex interplay of wind and surface currents in shaping the roughness of the sea surface that suggests the traditional Cox-Munk framework is not sufficient. In addition, the breaking crest length spectral density derived from visible and infrared imagery is shown to be modulated by the development of the wavefield (wave age) and alignment of wind and surface currents at the intermediate (dominant) scale of wave breaking.

1.   Introduction

[2] There is substantial complexity in the local wind-driven sea surface roughness microstructure, including very steep nonlinear wavelets and breakers. Nonlinear interfacial roughness elements: sharp crested waves, breaking waves as well as the active whitecap regions, passive foam, subsurface bubbles and spray they produce, contribute substantially to the distortion of the optical transmission through the air-sea interface. These common surface roughness features occur on a wide range of length scales, from the dominant sea state down to capillary waves. Traditional descriptors of sea surface roughness are scale-integrated statistical properties, such as significant wave height, mean square slope [e.g., *Cox and Munk*, 1954a, 1954b] and breaking probability [e.g., *Holthuijsen and Herbers*, 1986]. Wave breaking signatures range from large whitecaps with their residual passive foam, down to the centimeter-scale microscale breakers that do not entrain air. These numerous and diverse aspects of wave breaking are described in greater detail in review articles [e.g., *Banner and Peregrine*, 1993; *Melville*, 1996].

[3] Present state-of-the-art radiative transfer models [e.g., *Kattawar and Adams*, 1989; *Mobley*, 1994] (for a complete overview, see T. Dickey et al. (Recent advances in the study of optical variability in the near-surface and upper ocean, submitted to *Journal of Geophysical Research*, 2012) compute light transmission between the air and water side marine boundary layers. For light passing through the air-sea interface, these models rely heavily on the classical *Cox and Munk* [1954b, 1956] sea surface slope statistics, particularly the surface slope probability density function.

[1]Ocean and Climate Physics Division, Lamont-Doherty Earth Observatory, Columbia University, Palisades, New York, USA.

[2]School of Applied Mathematics, University of New South Wales, Sydney, New South Wales, Australia.

[3]Department of Computer Science, University of Massachusetts, Amherst, Massachusetts, USA.

[4]Physics and Astronomy, University of Victoria, Victoria, British Columbia, Canada.

[5]School of Mathematics and Statistics, University of New South Wales, Sydney, New South Wales, Australia.

[6]Department of Geography, Graduate Program in Marine Sciences, University of California, Santa Barbara, California, USA.

The rationale is that this statistical description adequately describes the ocean surface roughness. While this may suffice at modest wind speeds, it may not be optimal for stronger winds when wave breaking effects such as foam become more prevalent and modify the optical transmission and reflectivity of the sea surface.

[4] In this context, current knowledge of the sea surface roughness is incomplete. Only very limited spectral characterizations of open ocean wave height, slope and curvature have been measured to provide scale resolution for these geometrical sea roughness parameters [e.g., *Hara et al.*, 1998] and their modulational properties [e.g., *Hara et al.*, 2003]. Recently, field measurements of whitecap crest length spectral density [e.g., *Gemmrich et al.*, 2008; *Phillips et al.*, 2001] have been reported. These studies have been restricted to whitecapping gravity waves where the signature of wave breaking is captured by the optical contrast provided by the entrained air at the breaking crest. However, microscale breaking waves, which do not entrain air, can also impact the optical transmissivity of the ocean surface. To date, microscale breaker crest length spectral density measurements have been limited to the single laboratory study of *Jessup and Phadnis* [2005].

[5] In order to refine radiative transfer modeling capabilities, a more comprehensive prescription is needed of the sea surface roughness beyond the probability density function of the slopes. Wave height and slope spectra, and possibly the associated bispectrum which represents the wave nonlinearities, should be included in the modeling. Higher-order moments such as the curvature also need to be considered. Wave nonlinearity and breaking are also potentially important in creating surface geometry distortion, as well as attenuation and scattering of the light field. Envisaging a local lens equivalent of the surface topography indicates intuitively that these additional characterizations need to be included, but they are largely unknown at present.

[6] To address these goals, two intensive field experiments from R/P *Floating Instrument Platform* (*FLIP*) were staged in the Office of Naval Research's (ONR's) Radiance in a Dynamic Ocean (RaDyO) field program in the Santa Barbara Channel and in the central Pacific Ocean south of Hawaii (Dickey et al., submitted manuscript, 2012). Our measurements contribute key background sea state and environmental data for the RaDyO program. They also provide crucial wave height and wave slope validation data for verifying the fine-scale roughness measurements from our newly developed polarimetric camera. This instrument delivered new results for the mean square slope of the sea surface out to millimeter scales, as functions of, for instance, the time-varying wind speed/stress, underlying dominant sea state and ocean currents. In addition, our comprehensive video and infrared imagery provided concomitant statistical distributions of spectral density of whitecap crest length per unit area in different scale bands of propagation speed, and similarly for the microscale breakers.

[7] Previous studies tend to show heavily averaged properties of sea state, mean squared slope and breaking distributions. To our knowledge, no published studies to date investigate time-resolved variations with respect to the synoptic conditions. During RaDyO, the appreciable observation period and capacity to gather large data sets of multiple synoptic fields

(i.e., atmospheric, ocean, wave) provides an interesting opportunity to explore in detail how these short wave roughness fields respond to synoptic variables.

2. Experiments, Study Sites, and Platforms: Observational Programs Undertaken During RaDyO

[8] Two experiments defined the RaDyO program. The first field experiment was performed in the Santa Barbara Channel (SBC) from 3 to 25 September 2008. This setting was selected because it was expected to provide a relatively benign wind-wave state regime and easy access to shore since several new or prototype instrumentation systems were being utilized. The second RaDyO field experiment took place in the central Pacific Ocean south of Hawaii from 24 August to 15 September 2009. This location was selected because of its climatologically high, persistent wind speeds and sea states, its optically clear waters, and its open ocean character.

[9] Both experiments during RaDyO utilized R/P *FLIP* and the R/V *Kilo Moana*, a SWATH vessel. Both provide stable platforms for studies of meteorology, air-sea interaction, and physical oceanography. For the Santa Barbara Channel RaDyO experiment, R/P *FLIP* was moored in place at $34.2053°N$, $119.6288°W$ in water of depth 168 m using a two-point mooring (Figure 1). Some tilting of the R/P *FLIP* developed due to the currents and winds. In particular, R/P *FLIP* had a typical lean angle of 3–7° due to strong currents and about 0–5° due to wind forcing. These conditions were accompanied by a measurable oscillation in R/P *FLIP*'s heading with an approximately 2 min period. Instruments were deployed from R/P *FLIP*'s booms to minimize the influence of flow distortion and superstructure interference. The R/V *Kilo Moana* departed from Port Hueneme on 8 September 2008 and returned on 23 September 2008. For reference, R/V *Kilo Moana* sampled on station about 2 km north of R/P *FLIP* during the SBC experiment. For the central Pacific Ocean experiment south of Hawaii, R/P *FLIP* was freely drifting at a speed of 36.5 ± 8.2 cm s^{-1} to the west as shown in Figure 2. This anticipated high sea state experiment was carried out in the specific region of approximately 17.5° to 18.0°N, 155.5° to 160.0°W, south of the Hawaiian islands from 22 August to 14 September. The Kilo Mona left Sand Island, HI on 22 August and returned on 14 September. For most of this time it was in the designated experiment area, but for 2 days moved into the lee of the large island, to get protection from tropical storm Hilda, and to perform some calm seas/low wind experiments. Due to the passage of tropical storm Hilda, R/P *FLIP*'s departure from Pearl Harbor was delayed 5 days.

3. Measurement Systems

3.1. Instrument Deployment Overview

[10] Figure 3 shows the instrumentation deployed from the 20 m starboard boom on R/P *FLIP* during the field measurements in the Santa Barbara Channel and in the central Pacific Ocean south of Hawaii. An environmental monitoring system was deployed from the end of the boom that included a sonic anemometer, a water vapor sensor, a RH/T/
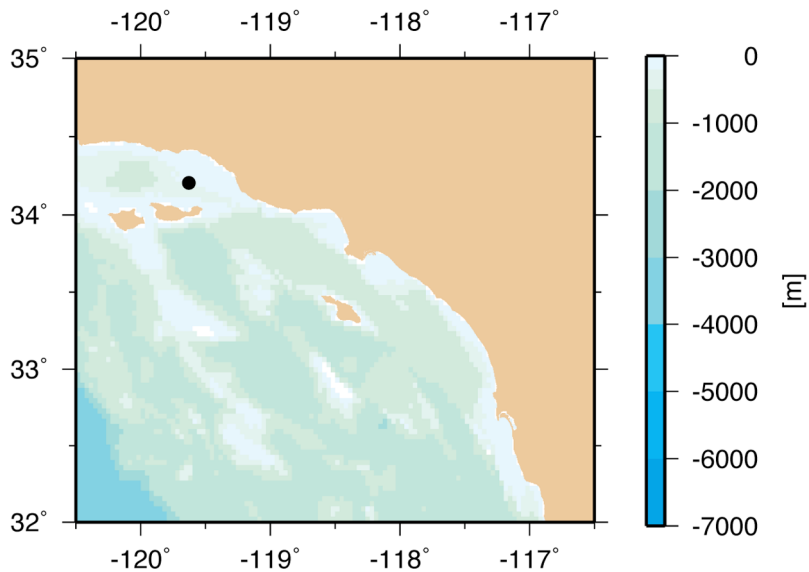
Figure 1. Mooring location of R/P *FLIP* (34.2053°N, 119.6288°W) using a two-point mooring in water of depth 168 m during the Santa Barbara Channel experiment.

P probe, a motion package, a pyranometer, and a pyrgeometer. Meteorological measurements included: near-surface barometric pressure, three-component wind velocity, relative and specific humidity, air temperature, longwave downwelling radiative flux, and shortwave downwelling irradiance. All sensors were mounted at nominally 10 m above sea level.

[11] Two orthogonal line scanning lidars, synchronized for zero crosstalk were deployed in addition to two laser altimeters. Two visible cameras were mounted at the end of
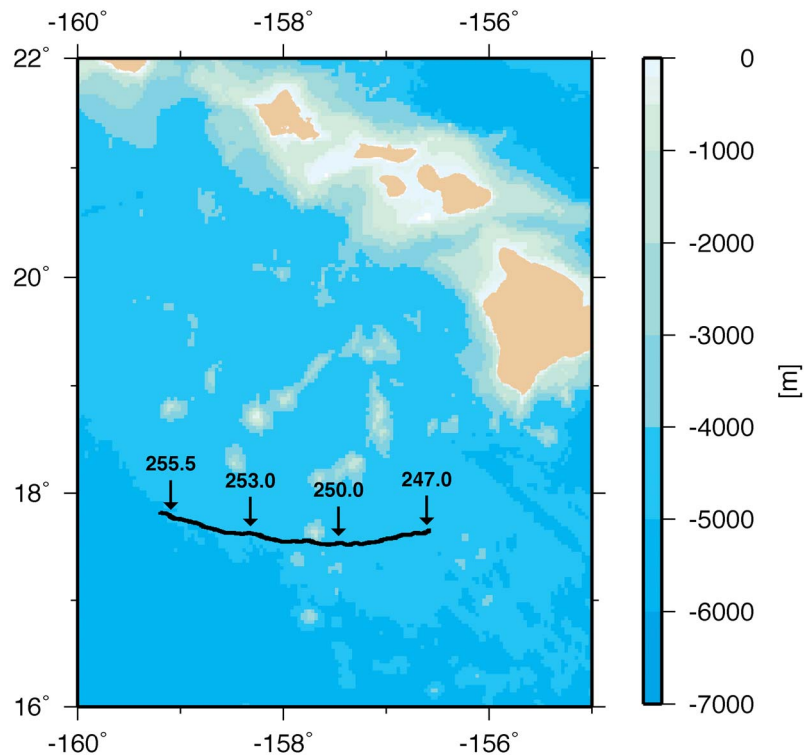

Figure 2. Drifting trajectory followed by R/P *FLIP* from 22 August to 14 September 2009 during the RaDyO experiment in the central Pacific Ocean south of Hawaii. The drift speed was 36.5 ± 8.2 cm s^{-1} toward the west. R/P *FLIP* started at 17.6515°N, 156.5640°W and finished at 17.8218°N, 159.1984°W.
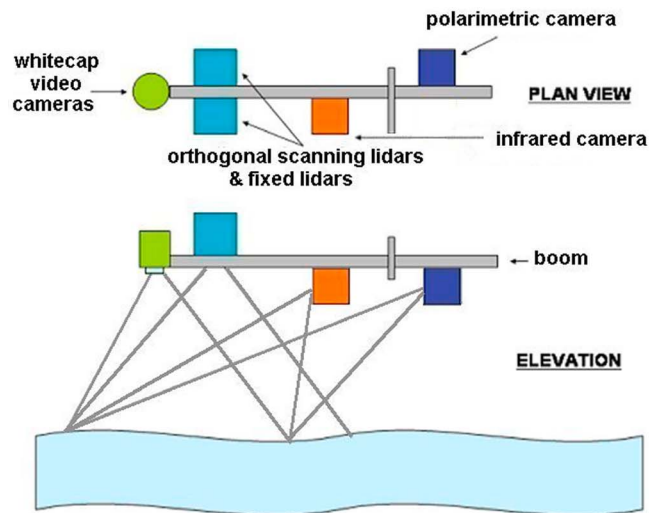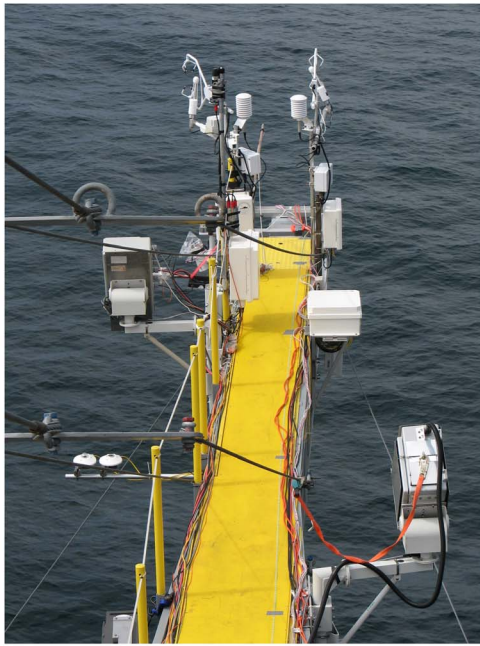
Figure 3. (top) The instrumentation setup deployed from the R/P *FLIP* starboard boom. (bottom) Schematic of the sea surface roughness instrumentation deployed packages. The end of the boom was about 9 m above the mean water level. The approximate field of view of the various instruments is shown. A second wide-angle whitecap video camera was mounted on R/P *FLIP* well above the boom to image the larger whitecaps.

the boom and viewed the water surface at nadir. The infrared (IR) camera system included a blackbody target and was mounted roughly 2.5 m from the end of the boom. A narrow field-of-view imaging polarimetric (POL) camera was deployed roughly 5.5 m from the end of the boom to quantify the very small-scale waves. The individual data acquisition systems were synchronized to GPS accuracy which allowed the various data sets to be interrelated to within 0.01 s. The IR and POL imagery were triggered at a frame rate of 60 Hz on the same pulse such that their timing

synchronization was better than 6 μs. Note that the POL and IR cameras were physically offset to account for the difference in nominal incidence angles of 20° for the IR and 37° for the POL camera. All the instruments (Visible/IR/POL imagery, scanning lidars, fixed laser altimeters) were positioned on the boom so that their intersection point was within a common footprint to measure small-scale surface roughness features and breaking waves. A third visible camera was mounted higher up in the crow's nest to provide a wider perspective on larger-scale breaking events. Complementary instrumentation deployed from R/P *FLIP* and R/V *Kilo Moana* is described by Dickey et al. (submitted manuscript, 2012), including hourly HF radar surface current maps of the Santa Barbara Channel. The radar data extend from the coast out to 120.6707°W and from 33.98°N to 34.56°N. They span the full month of September 2008 at hourly resolution, with areal resolution of 0.0218° (longitude) and 0.0180° (latitude).

3.2. Atmospheric Measurements

[12] Meteorological and direct covariance turbulent flux measurement systems were mounted on R/P *FLIP*. Direct covariance flux systems are capable of correcting for the velocity of platform motion [*Drennan et al.*, 1999; *Edson et al.*, 1998]. Measurement of the true vertical wind velocity is needed to compute the covariance fluxes. On the R/P *FLIP*, a Vaisala model CSAT-3 three-axis ultrasonic anemometer-thermometer and a Crossbow model VG400MA-100 system of three orthogonal angular rate sensors and accelerometers were used. The Crossbow was mounted directly beneath the sonic anemometer, allowing for accurate alignment with the sonic axes in addition to ensuring that the wind and motion measurements were collocated. During both RaDyO experiments, the micrometeorological system was deployed at the end of the 20 m starboard boom (Figure 3). This placed the anemometer 10 m above the mean sea surface.

[13] A fixed sensor package was deployed at the end of the R/P *FLIP* 20 m starboard boom for mean meteorological measurements. The sensor package was aspirated and included a combined RH-temperature and H_2O measurement. The RH-temperature sensor was a small Vaisala model HMP45. A Licor model 7500 open path NDIR sensor was also part of the shipboard meteorological system for measuring water vapor in the mean and fluctuations for the direct covariance technique. Longwave and shortwave radiation were measured by Kipp and Zonen models CGR-4 pyrgeometer and CMP-21 pyranometer, respectively. Barometric pressure was supplied by the Vaisala model PTB110.

3.3. Fixed and Linear Scanning Laser Altimeters

[14] A compact, portable wave measurement system (SICK model LMS291-S14) was used; it is based on scanning lidar technology capable of measuring the dominant sea state from R/P *FLIP* and from the R/V *Kilo Moana.* We deployed two orthogonal line scanning lidars from R/P *FLIP*, synchronized for zero crosstalk. We also deployed two Riegl model LD90-3100VHS laser altimeters. These were mounted at the end of the 20 m starboard boom, as part of our team's comprehensive surface roughness instrumentation package. This arrangement is shown in Figure 3

(bottom). A third scanning lidar was deployed on the R/V *Kilo Moana*. We fitted our predesigned boom between the bows on the front of the R/V *Kilo Moana* during the SBC experiment. There was some concern about the effect of dolphins surfing in the data collection area on the R/V *Kilo Moana* lidar, and affected data were removed. Since most subsurface optical measurements were from the rear deck of the R/V *Kilo Moana*, in the Hawaii experiment the lidar was deployed from the rear deck to record the wave height conditions in closer proximity to where the optical measurements were being made. Hence during the Hawaii experiment, the R/V *Kilo Moana* lidar data monitored the wavefield as influenced by the ship wake in which the subsurface optical data were collected. Also, in this deployment the lidar was closer to the water surface and hence the instrument suffered heavy spray and dunking on a number of occasions.

[15] The SICK scanning lidars had a scan rate of 75 Hz (all processing was downsampled with averaging to 15 Hz), transmitting a light pulse every $0.5°$ over a $90°$ quadrant. When deployed to look downward from 9 m above MSL (as on R/P *FLIP*), scanning $\pm 45°$ about nadir, the local sampling region for the beam was about 150×50 mm in the along-track and cross-track directions. This arrangement allowed scanning along a line up to 10 m long, depending on the presence of specular scatterers. The minimum wavelength resolvable was $O(300$ mm), with a corresponding root-mean-square (RMS) height resolution of about ± 10 mm and an accuracy of ± 35 mm. The Riegl laser altimeters sampled at 50 Hz, with a beam divergence of 3 by 0.5 mrad that corresponds to a beam width of 30 by 5 mm at 10 m range. The measurement accuracy is ± 25 mm and the measurement resolution is ± 25 mm. The wave height data gathered addressed the requirements for both our team's efforts on sea surface roughness characterization as well as providing communal sea state data for all RaDyO PI's.

[16] The fixed and scanning lidars operated continuously throughout the field experiments. Their data were used to obtain wave spectra and other wave statistics including significant wave height and dominant wave frequency. In addition, the orthogonal linear scanning lidar system provided spatiotemporal properties (interlaced *x-z* and *y-z* scans) of the wave height field resolved to the order of 0.5 m wavelengths. These measurements provide the phase of polarimetric, infrared and visible camera imagery (described below) of surface microstructure needed for quantifying short wave modulation with respect to the underlying dominant wind waves.

3.4. Polarimetric Imaging

[17] In cooperation with Polaris Sensor Technologies and led by Howard Schultz, we designed and built an imaging polarimeter specifically for oceanographic applications. The commercial off-the-shelf (COTS) imaging polarimeter used for the preliminary work described by *Zappa et al.* [2008] was not suitable for general oceanographic applications for two reasons. The imaging speed of the COTS polarimeter was too slow. Integration times on the order of 17 ms were required to collect data. In an open ocean environment, where small waves are advected by ocean swell, a 17 ms integration time would result in unacceptable motion blur. In

addition, the COTS polarimeter frame rate of 15 frames s^{-1} was too slow to capture the temporal history of small waves.

[18] Commercial off-the-shelf imaging polarimeters typically are modified RGB cameras where the red, green and blue filters are replaced with linear polarization filters oriented at $0°$, $45°$, and $90°$. Since polarizing filters typically pass approximately 20% of the light, using filters to take polarization images is an inherently inefficient process. Instead of using filters, the Polaris Sensor Technologies (PST) design incorporates a proprietary beam splitter design that separates the polarization components. As a result, the PST design is approximately 97% efficient, which allowed us to operate with integration times on the order of 1 ms.

[19] The beam splitter design does not produce a pure polarization state at each exit aperture. Instead, the light at each exit aperture contains a linear combination of the four Stokes components. At the time of assembly, a calibration procedure measures the amount of each polarization component present at each aperture. A data reduction matrix is found that transforms the mix of polarization states to the four Stokes parameters.

[20] To achieve a 60 Hz frame rate, the PST design uses one JAI monochrome digital camera (model CV-A10CL M) at each of the four exit apertures. The JAI cameras incorporate a Sony ICX415 1/2 inch monochrome CCD sensor. The image format is 768×576 pixels, the pixel depth is 10 bits, and the maximum frame rate is 60 Hz noninterlaced. The imaging polarimeter was deployed in a water-resistant housing from the starboard boom 9 m above the surface. The sensor was oriented so that it observed the ocean surface at a $37°$ incidence angle. The instrument was equipped with a $4.8° \times 3.6°$ field-of-view lens. The nominal horizontal extents of the image footprint on the ocean surface (*x* direction) are 0.9600, 0.9848, and 1.0120 m at the bottom, middle, and top of the image, respectively. The nominal vertical extent of the image (*y* direction) is 0.9646 m. The corresponding horizontal pixel scale is 1.25, 1.28, and 1.32 mm at the bottom, middle, and top of the image; and a corresponding vertical pixel height of 1.68 mm at the image center.

3.5. High-Resolution Visible and Infrared Imaging

[21] We deployed a moderate field-of-view CEDIP model JADE 570 LWIR IR camera and two digital video cameras (one Prosilica model GC1380 and one Imperx model IPX-1M48-L) from R/P *FLIP*'s starboard boom, and a third digital video camera (Prosilica model GC1380) from the crow's nest 26 m above MSL. The IR camera measured thermal radiation from 7.7 to 9.3 μm emitted by the ocean surface using a 320 by 240 MCT focal plane array with 14 bit digitization sampled at 60 Hz. The IR system includes a uniform target blackbody for the calibration and nonuniformity correction of the MCT array detector. Resulting temperature resolution was $0.02°$C and calibration was better than $0.05°$C. The three digital visible CCD cameras recorded images sampling at 20 Hz, two at 1024×1360 resolution (Prosilica model GC1380) and 12 bit digitization depth, and one at 1000×1000 resolution with 12 bit digitization depth. The IR and visible camera images were postprocessed to compute statistics on the scale, frequency, and speed of microbreaking and whitecapping

events from scales of order 0.1 m s^{-1} up to scales of order 10 m s^{-1}. In particular, these data were used for determining breaking crest length spectral density distributions and their higher moments.

[22] The three cameras were used to observe wave breaking, foam, and whitecapping over fields of 10 by 15 m (2 cameras) and 100 by 200 m (1 camera). The former cameras were mounted near the fixed and scanning lidar systems close to the end of a boom (~9 m height) to measure intermediate scale breakers while the other was mounted on R/P *FLIP*'s crow's nest at about 26 m above water level for a broader viewing angle to record larger scale breaking events. The sampling rates for all cameras were either 10 or 20 Hz. Data were generally collected for 20 min every hour during daylight hours; however, data were recorded more often during periods of more frequent wave breaking events. Overall, 37 h over 13 days were recorded during the SBC experiment and 21 h over 5 days were recorded during the experiment south of Hawaii. The individual data acquisition systems were synchronized to GPS accuracy which allowed the IR and visible imagery data sets to be interrelated to within 0.01 s.

3.6. Ocean Skin Temperature Measurements

[23] A longwave narrow field-of-view Heitronics model KT-15.82 LWIR radiometer (8–14 μm) was directed skyward to discriminate real from apparent ocean surface temperature variability during both field experiments from R/P *FLIP*. During the Santa Barbara Channel experiment, we used the skyward radiometer at 20° zenith angle in combination with the JADE camera at 20° incidence angle to determine the skin temperature. During the Hawaii experiment, we deployed a second Heitronics model KT-15.82 radiometer that viewed the ocean surface at an incidence angle of 25° with the skyward radiometer at 25° zenith angle. The combination of Heitronics skyward and downward looking radiometers provided a continuous time series of skin temperature, in addition to the random samples of skin temperature made by the JADE camera. We use the method outlined in equation (A2) of Appendix A of *Zappa et al.* [1998] to calculate the skin temperature.

4. Results and Discussion

4.1. Ambient Environmental Conditions

[24] The general wind pattern in Southern California during summer is determined by the position and strength of the subtropical anticyclone (i.e., surface high-pressure system) over the eastern North Pacific. In addition, a surface thermal low-pressure system usually forms over the southwestern U.S. in late summer or early autumn, and plays a significant role in modifying horizontal pressure gradients and wind regimes in central and southern California [e.g., *Dorman and Winant*, 1995; *Winant and Dorman*, 1997]. Many studies have extensively investigated the dynamics of atmospheric circulations in the SBC during summertime [e.g., *Dorman and Winant*, 1995, 2000; *Dorman and Koračin*, 2008; *Skyllingstad et al.*, 2001; *Winant and Dorman*, 1997]. The typical summer day is marked by strong northwesterly winds off the western coast of southern California. As the winds turn at Point Conception (34.449°N, 120.471°W) and

enter the SBC, there is a significant increase in speeds from 5 m s^{-1} over Point Conception to 10 m s^{-1} over the western part of the SBC [*Skyllingstad et al.*, 2001]. Wind speeds then decrease rapidly (~3 m s^{-1}) over the eastern part of SBC and winds turn westerly. Significant diurnal variations exist in the atmospheric circulation and marine boundary layer (MBL) associated with synoptic conditions, hydraulic flow, thermal effects, land-sea breeze circulations and sea surface temperature gradients in the channel [*Skyllingstad et al.*, 2001].

[25] The atmospheric conditions during the experiment were important for the physical forcing in terms of waves, mixing, and currents as they all influence the temporal and spatial variability of the optical properties and the subsurface light fields. A summary of the environmental conditions observed during the Santa Barbara Channel study is shown in Figure 4. Throughout this paper all times are given as UTC, using the yearday definition: 1 January, noon = yearday 1.5. Mean surface winds were systematically from the northwest in the region near Point Conception with little diurnal variation in direction and slight changes in intensity. In contrast, mean surface winds in the eastern SBC were primarily from the west with small variations in direction but with considerable changes in intensity. The SBC experiment experienced a variety of conditions with generally low winds in the early morning with mean wind speed of 4.8 ± 2.7 m s^{-1} (all plus/minus bounds refer to a combination of natural variability and measurement uncertainty as expressed by the standard deviation), and strong sea breezes up to 12 m s^{-1} in the evening with mean wind speeds of 7.1 ± 2.2 m s^{-1}. The data show a distinctive and persistent diurnal structure to the wind speed that was stronger in the afternoon relative to the night and morning. Wind speed referenced to 10 m, U_{10}, for the whole experiment was 5.8 ± 2.5 m s^{-1}. The solar incidence, bulk air temperature, relative humidity, and ocean skin temperature show obvious diurnal cycles. The solar incidence showed peaks of up to 861 W m^{-2}. Relative humidity ranged between 75% and 94% with an average value of 86.5 ± 3.6%, air temperature ranged between 15.8° and 18.4° with an average value of 16.8 ± 0.5°, and ocean skin temperature ranged between 15.9° and 21.1° with an average value of 18.3 ± 1.0°. The barometric pressure indicates a semidiurnal cycle with an average value of 101.2 ± 0.1 kPa. The downwelling longwave radiation shows that the conditions were relatively clear (310–340 W m^{-2}) for most of the experiment with periods of cloudiness (near 400 W m^{-2}) that occurred predawn and in the early morning on days 258 and 265–268. For the purposes of further discussion, the data is separated into three regimes: days 257–259, 260–263, and 264–268. The wind speed for these three regimes was 5.5 ± 2.4, 7.6 ± 1.8, and 4.1 ± 2.1 m s^{-1}, respectively. The diurnal cycles for bulk air temperature, relative humidity, and ocean skin temperature were strongest during the third regime and less intense earlier in the experiment.

[26] The location of the RaDyO experiment in the central Pacific Ocean experiment south of Hawaii was selected because of its climatologically high, persistent wind speeds, its well-developed wavefield with strongly forced sea states, its optically clear waters, and its open ocean character with a
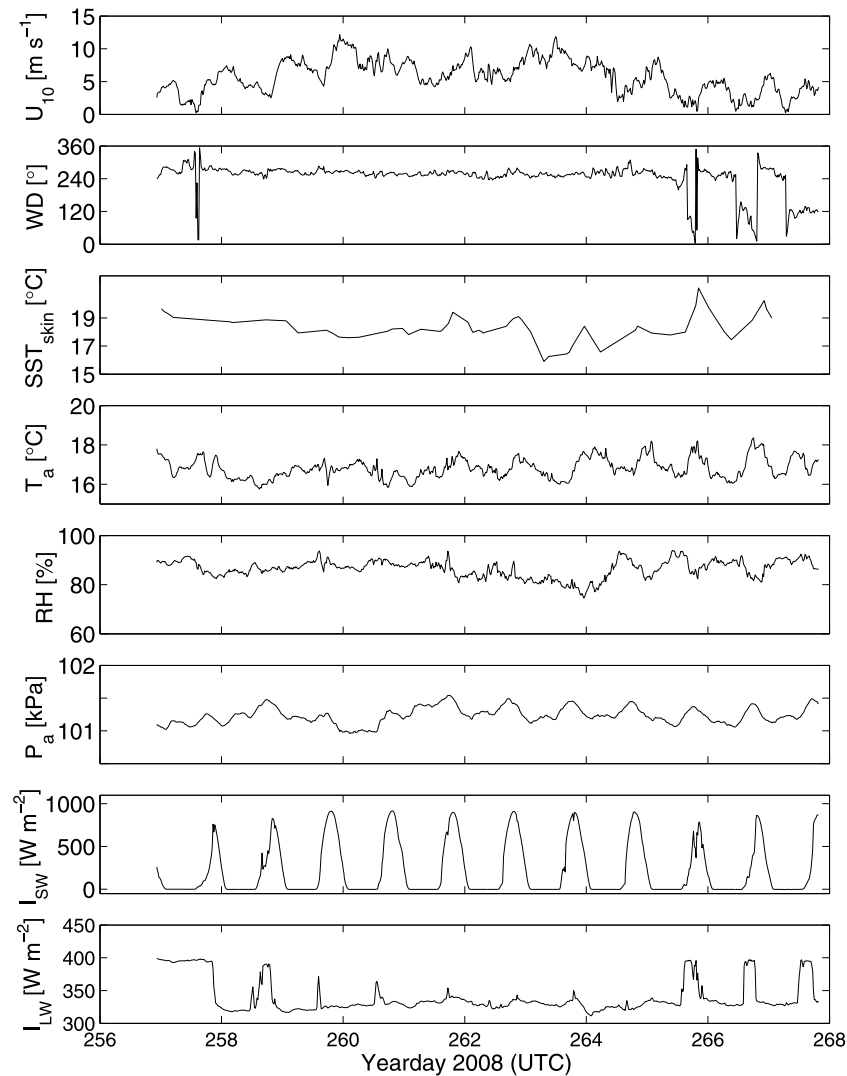
Figure 4. Time series of wind speed, U_{10}; wind direction, WD; ocean skin temperature, SST_{skin}; air temperature, T_a; relative humidity, RH; barometric pressure, P_a; incoming solar radation, I_{sw}; and downwelling longwave radiation, I_{lw}, during the Santa Barbara Channel experiment. Wind direction follows the atmospheric convention of "from."

well-known oceanic and atmospheric climatology. The Hawaiian RaDyO study region lies in the subtropical North Pacific gyre. The clockwise wind pattern of the subtropical North Pacific gyre has been documented in several studies [e.g., *Hellerman and Rosenstein*, 1983; *Wyrtki and Meyers*, 1976]. The wind patterns of the Hawaiian RaDyO study region generally vary from northeasterly to easterly and display some seasonality with maximum trade winds occurring in summer months and more moderate winds during winter. The wind-driven currents in the RaDyO study region lie on the southern side of this gyre and are part of the North Equatorial Current (NEC). The surface currents of the NEC are directed predominantly from east to west in latitudes of roughly $10°$ to $20°N$ and thus through our RaDyO study site. The NEC has been described in several papers [e.g., *Munk*, 1950; *Wyrtki*, 1974], and its position is generally correlated with the atmospheric Intertropical Convergence Zone (ITCZ).

[27] A summary of the environmental conditions observed during the central Pacific Ocean experiment south of Hawaii is shown in Figure 5. The Hawaii experiment experienced a variety of conditions with generally moderate winds throughout. The data show a distinctive and persistent decrease in the easterly wind speed from 10.2 m s^{-1} at the beginning of the experiment to 8.5 m s^{-1} at the end. Wind speed for the whole experiment was 9.1 ± 1.1 m s^{-1}. The solar incidence showed an obvious diurnal cycle with peaks at 1004 W m^{-2}, and the bulk air temperature showed more subtle diurnal cycle. Relative humidity ranged between 68% and 91% with an average value of $86.1 \pm 3.9\%$, air temperature ranged between $25.2°$ and $26.9°$ with an average value of $26.2 \pm 0.3°$, and ocean skin temperature ranged between $26.0°$ and $27.4°$ with an average value of $26.8 \pm 0.4°$. The barometric pressure indicates a strong semidiurnal cycle with an average value of 101.3 ± 0.1 kPa. The downwelling longwave radiation shows that the conditions

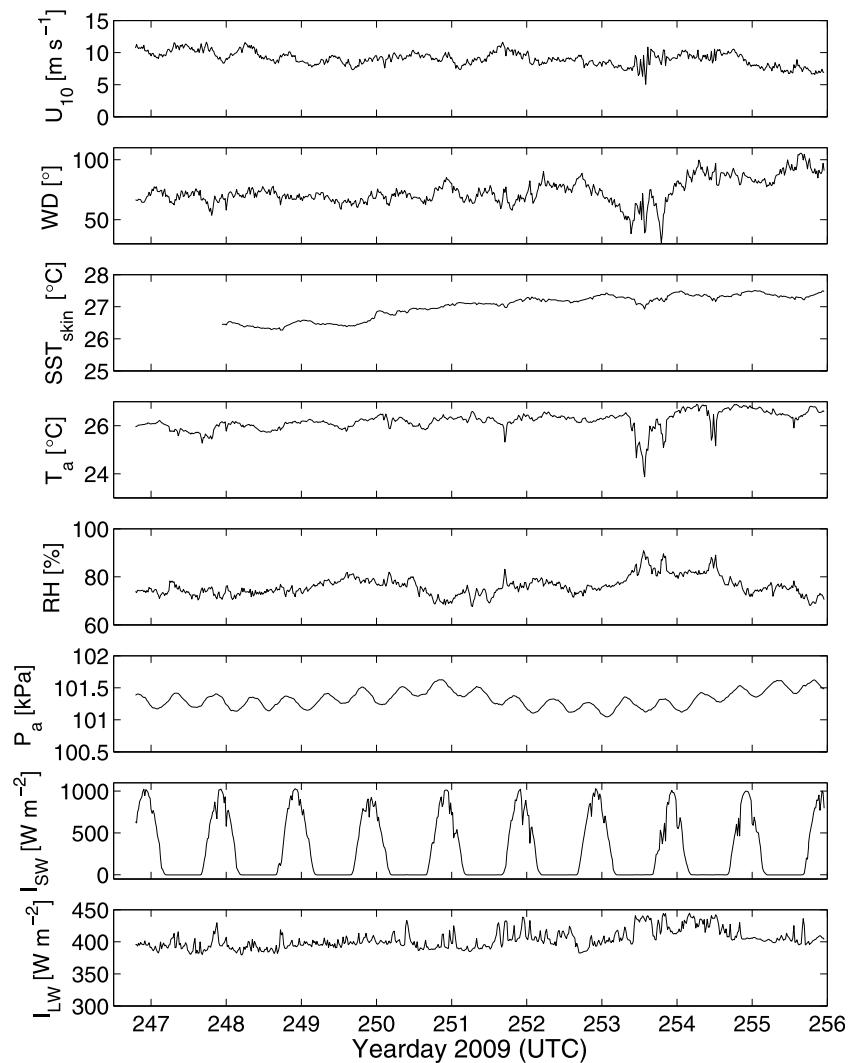**Figure 5.** Time series of wind speed, U_{10}; wind direction, WD; ocean skin temperature, SST_{skin}; air temperature, T_a; relative humidity, RH; barometric pressure, P_a; incoming solar radation, I_{sw}; and downwelling longwave radiation, I_{lw}, during the central Pacific Ocean experiment south of Hawaii. Wind direction follows the atmospheric convention of "from."

were partly cloudy (380 to 445 W m^{-2}) throughout the experiment. Note that on day 253, the wind speed, air temperature and relative humidity all experience sudden and rapid variability that is due to the rain which contaminates the measurement signal. The data from these short durations have been removed.

4.2. Air-Sea Flux Conditions

[28] The flux determined by the micrometeorological methods assumes stationary conditions over the measurement period and knowledge of the atmospheric boundary layer stability. The inferred fluxes are critically dependent on these assumptions. The stationarity criteria for micrometeorological fluxes will be violated if there are significant horizontal gradients in the air over the area of measurements [*Businger and Delaney*, 1990]. This requires the signal averaging duration to correspond to as much as 50 km. The islands and mainland during the SBC experiment, and storm

fronts during the Hawaii experiment may both violate this assumption, although the measurements are likely reasonable at 10 km range.

[29] The corrected velocity components are used to compute the covariance fluxes of momentum, sensible heat, and water vapor. The momentum flux is described by

$$\tau = -\rho \overline{u'w'}, \tag{1}$$

where the overbar represents a time average quantity (20 min), ρ is the density of moist air, and u and w are the longitudinal and vertical wind velocity components, respectively. In this expression, u' and w' represent the turbulent fluctuations. The surface friction velocity can be derived from the direct covariance by

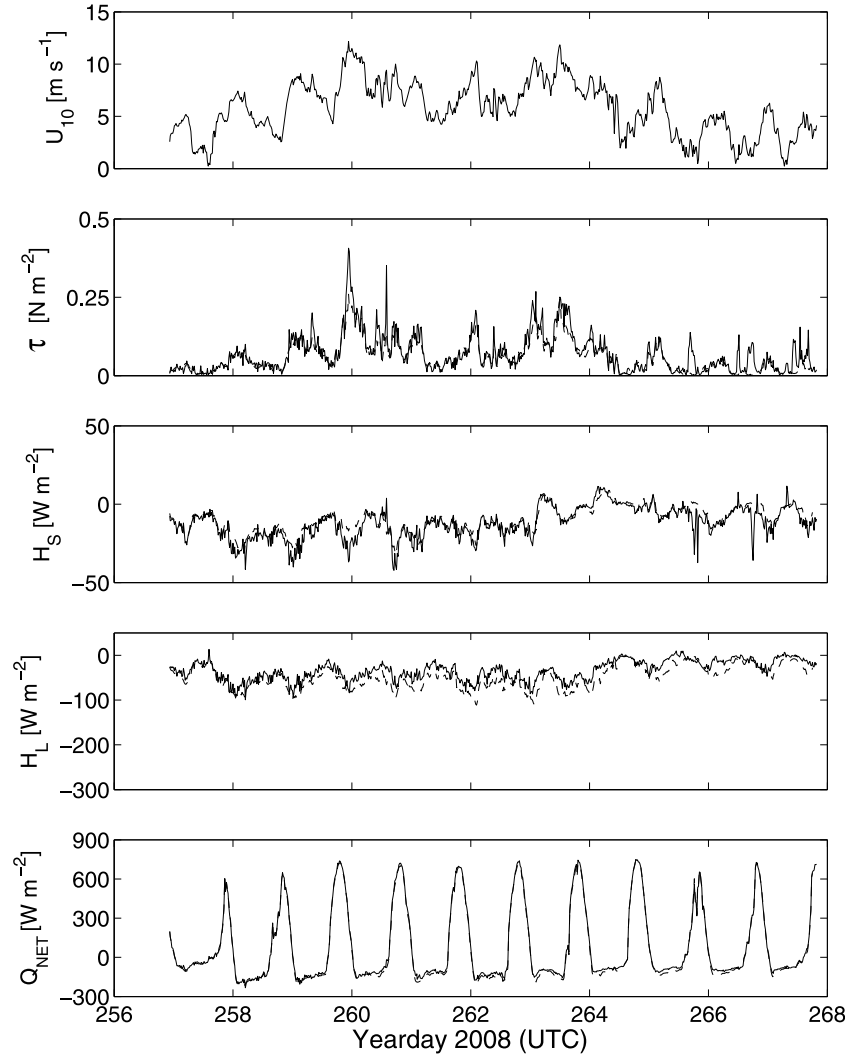$$u_* = \left(-\overline{u'w'}\right)^{1/2}. \tag{2}$$

Figure 6. Time series of wind speed, U_{10}; momentum flux, τ; sensible heat flux, H_s; latent heat flux, H_l; and net heat flux, Q_{net}, during the Santa Barbara Channel experiment. Solid lines use direct covariance measurements and dashed lines use TOGA-COARE bulk fluxes.

[30] The turbulent air-sea fluxes for sensible, H_s, and latent, H_l, heat can also be measured using w' with fluctuating temperature and water vapor concentrations, giving

$$H_s = \rho c_p \overline{w'T'} \qquad (3)$$

and

$$H_l = \rho L_E \overline{w'q'}, \qquad (4)$$

where c_p is the specific heat for moist air, L_E is the water latent heat of vaporization, T is the air temperature, and q is the specific humidity. The CSAT3 sonic anemometer measures temperature based on the speed of sound, which is a function of density; hence the result must be corrected for water vapor. The sensible heat flux is determined following *Dupuis et al.* [1997] by $\overline{w'T'} = \left(\overline{w'T'}_{sonic} - 0.518T\overline{w'q'} \right)/(1 + 0.518q)$, where T_{sonic} is the measured sonic temperature. The net heat flux, Q_{net}, is the sum of H_s, H_l, net longwave radiation, Q_{lw}, and net solar radiation, Q_{sw}. The net longwave radiation is defined as $Q_{lw} = \varepsilon_{si} (I_{lw} - \sigma_b SST_{skin}^4)$ and the net solar radiation

is defined as $Q_{sw} = [1 - a_s (\tau_{es})]I_{sw}$ where I_{lw} is the longwave irradiance measured by the pyrgeometer, ε_{si} is the spectrally integrated emissivity as a function of temperature based on *Downing and Williams* [1975], σ_b is the Stefan-Boltzmann constant, SST_{skin} is the ocean skin temperature, a_s is the albedo using *Payne* [1972] that is a function of atmospheric transmittance, τ_{es}, and I_{sw} is the shortwave irradiance measured by the pyranometer.

[31] Time series of momentum (wind stress), sensible heat, and water vapor direct covariance fluxes during the Santa Barbara Channel study are shown in Figure 6. Also shown are the Tropical Ocean–Global Atmosphere (TOGA)-Coupled Ocean-Atmosphere Response Experiment (COARE) model bulk fluxes [*Fairall et al.*, 2003]. The flux variability was caused by environmental forcing and measurement uncertainty. Diurnal processes were the origin of most of the variability in the atmospheric and oceanic forcing. The momentum, sensible heat, and latent heat fluxes all show a diurnal cycle similar to the wind speed. The average momentum flux for the whole experiment was 0.070 ± 0.061 N m^{-2}, while the momentum flux during the three

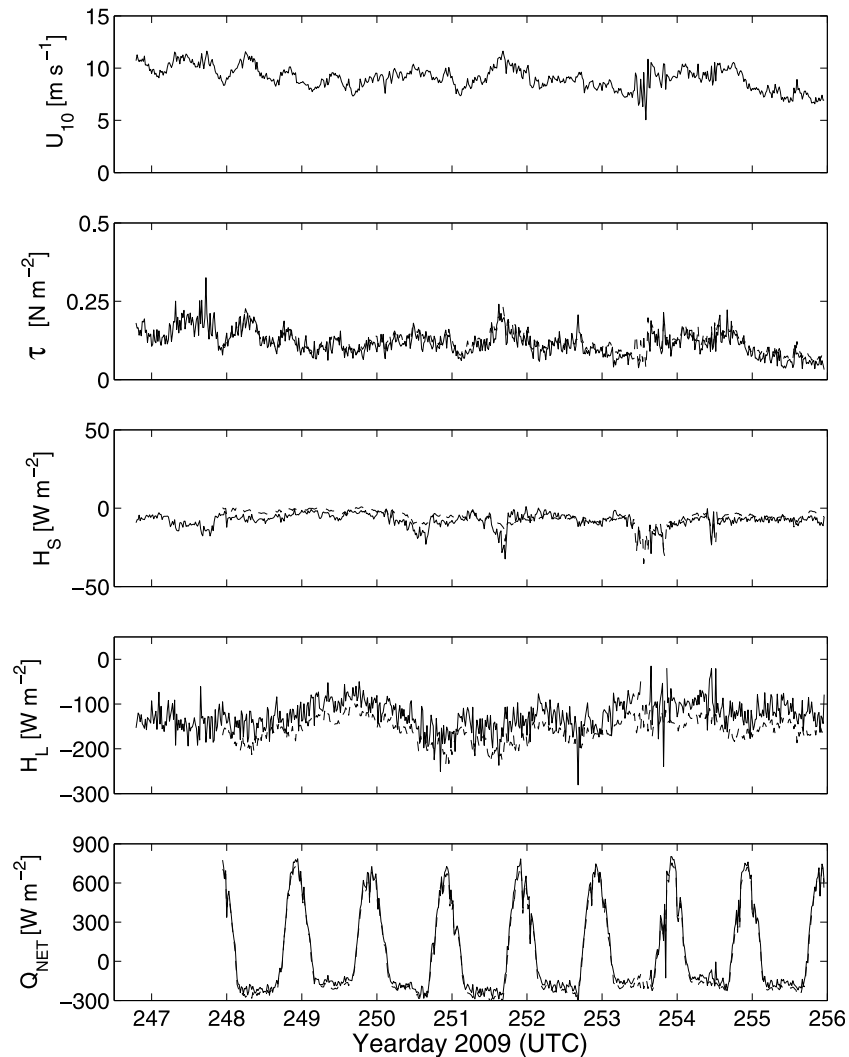**Figure 7.** Time series of wind speed, U_{10}; momentum flux, τ; sensible heat flux, H_s; latent heat flux, H_l; and net heat flux, Q_{net}, during the central Pacific Ocean experiment south of Hawaii. Solid lines use direct covariance measurements and dashed lines use TOGA-COARE bulk fluxes.

regimes 0.062 ± 0.064 (days 257–259), 0.104 ± 0.062 (days 260–263), and 0.042 ± 0.035 N m^{-2} (days 264–268). The most significant diurnal process came from the sea breeze. Strong diurnal heating of the California central valley and high desert created a low atmospheric pressure over land, which accelerated the westerly gradient wind during the afternoon and evening. Large radiative cooling of the dry soil in clear skies leads to significant cooling of the terrestrial nighttime atmosphere, and consequently the pressure gradient decreases. This leads to diurnal variations in wind speed, and hence wind stress, momentum flux and sea state. The surface ocean is heated during the day by incident solar radiation. At night, when solar radiation is nonexistent, infrared radiation, evaporation, and sensible heat fluxes cool the ocean surface. These processes vary through the diurnal cycle and cause subsequent processes that change the transport of heat, mass, and momentum across the air-sea interface. The diurnal barometric pressure changes are small. Thus, the time series of direct covariance measurements are close to a uniform daily mean and banded

around variability caused by noise and diurnal forcing. The mean and standard deviation of the sensible and latent heat direct covariance fluxes were -13.9 ± 10.7 and -33.9 ± 21.8 W m^{-2}. Note that the standard deviations of the measured 0.5 h direct covariance fluxes are often as large as the mean fluxes. For days 258–263, the mean sensible heat flux was -20.8 ± 8.8 W m^{-2}, the mean latent heat flux was -45.6 ± 17.2 W m^{-2}, and the mean net cooling at night was -125.6 ± 38.5 W m^{-2}. During regime three between days 264 and 268, the mean sensible heat flux was -6.4 ± 7.8 W m^{-2}, the mean latent heat flux was -21.7 ± 19.9 W m^{-2}, and the mean net cooling at night was -89.3 ± 16.5 W m^{-2}. The peak warming throughout the experiment ranged between 600 and 750 W m^{-2}.

[32] Time series of momentum (wind stress), sensible heat, and water vapor direct covariance fluxes during the central Pacific Ocean study south of Hawaii are shown in Figure 7. Similar to the wind speed, the momentum flux shows a slow decrease from 0.16 N m^{-2} at the beginning of the experiment to 0.10 N m^{-2} at the end. The average

momentum flux for the whole experiment was 0.118 ± 0.041 N m^{-2}. Again, the most significant diurnal process is the heating and cooling of the ocean surface. The mean and standard deviation of the sensible and latent heat direct covariance fluxes were -15.1 ± 5.46 and -126.9 ± 32.2 W m^{-2}. The mean net cooling at night throughout the experiment was -190.2 ± 43.35 W m^{-2}. The peak warming throughout the experiment ranged between 600 and 780 W m^{-2}. Note that on day 253, rain contaminated all the direct covariance fluxes, including the net heat flux.

[33] The RaDyO flux data tracks the TOGA-COARE 3.0 model prediction closely. The measured sensible heat flux is within 1.1 W m^{-2} of the TOGA-COARE 3.0 model prediction for SBC and within 2.1 W m^{-2} for the Pacific Ocean south of Hawaii. The TOGA-COARE 3.0 model prediction overestimates the measured latent heat flux by at most 31.6% for SBC and 21.8% for the Pacific Ocean south of Hawaii. *Edson* [2008] has observed similar tendencies of this magnitude in his extensive data sets including Clivar Mode Water Dynamic Experiment (CLIMODE), Coupled Boundary Layer and Air-Sea Transfer (CBLAST) Experiment, Marine Boundary Layer (MBL) Experiment, and Risø Air-Sea Experiment (RASEX). He is incorporating these observations into the latest TOGA-COARE 4.0 model transfer coefficients where the Dalton number needs to be reduced by up to 25% for winds below 10 m s^{-1} [see *Edson*, 2008, Figure 8]. Thus, the greater overestimation observed in SBC for the latent heat flux is consistent with the larger corrections at lower wind speeds proposed by *Edson* [2008]. Our observations during the RaDyO experiments in SBC and in the Pacific Ocean south of Hawaii provide independent validation of these effects.

[34] We note that the dynamic range of the wind stress is larger during the SBC experiment than the Hawaii experiment. Together these two experiments provide an interesting variety of sea state conditions including light and variable to strongly whitecapping. They provide a valuable test bed for mean square slope and breaking measurements over an interesting dynamic range of wind speeds.

[35] The results presented here document the underlying conditions to support the optical measurements gathered during RaDyO. The short duration of the RaDyO observational periods results in too few data to refine or comment on the flux parameterization relationships. Much longer records would have been needed to compare the transfer coefficients (Stanton and Dalton numbers) in the coastal versus open ocean settings.

4.3. Wave Conditions

[36] Our comprehensive wave measurement system was deployed from R/P *FLIP* during the first intensive observational experiment in September 2008 in the Santa Barbara Channel. A moderate range of sea state conditions prevailed. The wind speed, U_{10}, ranged from light and variable, up to 12 m s^{-1} and the significant wave height ranged from 0.7 to 2.0 m and showed strong diurnal variations. Figure 8 shows a summary of the wind speed and wave heights measured during September 2008. This information characterizes the background environment experienced by the short wind waves (the sea surface microstructure roughness) measured by the POL and IR imagery. The seas were complex, with

swells propagating around and through the islands, and young wind seas evolving on the intersecting swells. Figure 8 shows the strong correspondence between changes in the wave height and wave spectra with changes in the wind speed (and also the wind stress shown in Figure 6). These sea state changes are clearly associated with the prevailing strong diurnal wind forcing in this region.

[37] In marked contrast, during 23 August to 16 September 2009 south of Hawaii in the central Pacific Ocean, a far more moderate range of sea state conditions occurred; the wind speed, U_{10}, steadily decreased from 12 to 8 m s^{-1} and the significant wave height ranged from 1.7 to 2.7 m. Figure 9 shows a summary of the wind speed and wave heights measured south of Hawaii. During the Hawaii experiment, the seas were dominated by wind seas generated by the easterly trade winds, although some intermediate swells generated by regional thunderstorms and squall lines were also seen during the experiment. The data show a distinct decrease in wind speed and a persistent wave energy that was higher than during the Santa Barbara Channel experiment.

[38] Figure 10 shows typical scanning lidar data during the SBC experiment. Figure 10 (top) shows the instantaneous signal along a typical single scan line and the interpolated smooth spline. Figure 10 (middle) shows the corresponding local wave slope along the scan line produced by differentiating the interpolated data in Figure 10 (top). The time series of the nadir elevation gives the information equivalent to a fixed wave wire, and this can be transformed to give the wave frequency spectrum. This information is shown in Figure 10 (bottom) for the waves measured simultaneously by the lidars from R/P *FLIP* and from the R/V *Kilo Moana*. The sea breeze generated a strong local wind sea as is seen in both the R/V *Kilo Moana* and R/P *FLIP* spectra. This sea breeze was superimposed on a persistent westerly wind that left the wind-driven sea state free of strong directional complexity. However, young swell from the southwest propagated around and between the Santa Barbara Channel Islands that enclose SBC before reaching our observation area. The R/V *Kilo Moana* and R/P *FLIP* were 2 to 3 km apart during these observations. These young swells are locally inhomogeneous because of the complex refraction about the islands and we attribute the difference at low frequencies in the spectra to such local effects.

[39] During the SBC deployment, the R/V *Kilo Moana* lidar was mounted on the bow of the ship and was unaffected by the ship wake effects. It is evident that these wavefields match closely and assured that the optical measurements were being made in similar wave environments from R/P *FLIP* and from the R/V *Kilo Moana* which were sometimes separately by several kilometers. However, we note that during the experiment south of Hawaii, the R/V *Kilo Moana* lidar was mounted on the stern of the vessel. These wave data were representative of the local sea surface conditions colocated with the optical measurements made from stern of the R/V *Kilo Moana*. During the field experiments, two scanning lidars operated from R/P *FLIP*, measuring the large-scale wave geometry (height and slope components). These measurements were collocated with our polarimeteric, infrared and optical imaging systems collecting the high-resolution surface roughness data described below.
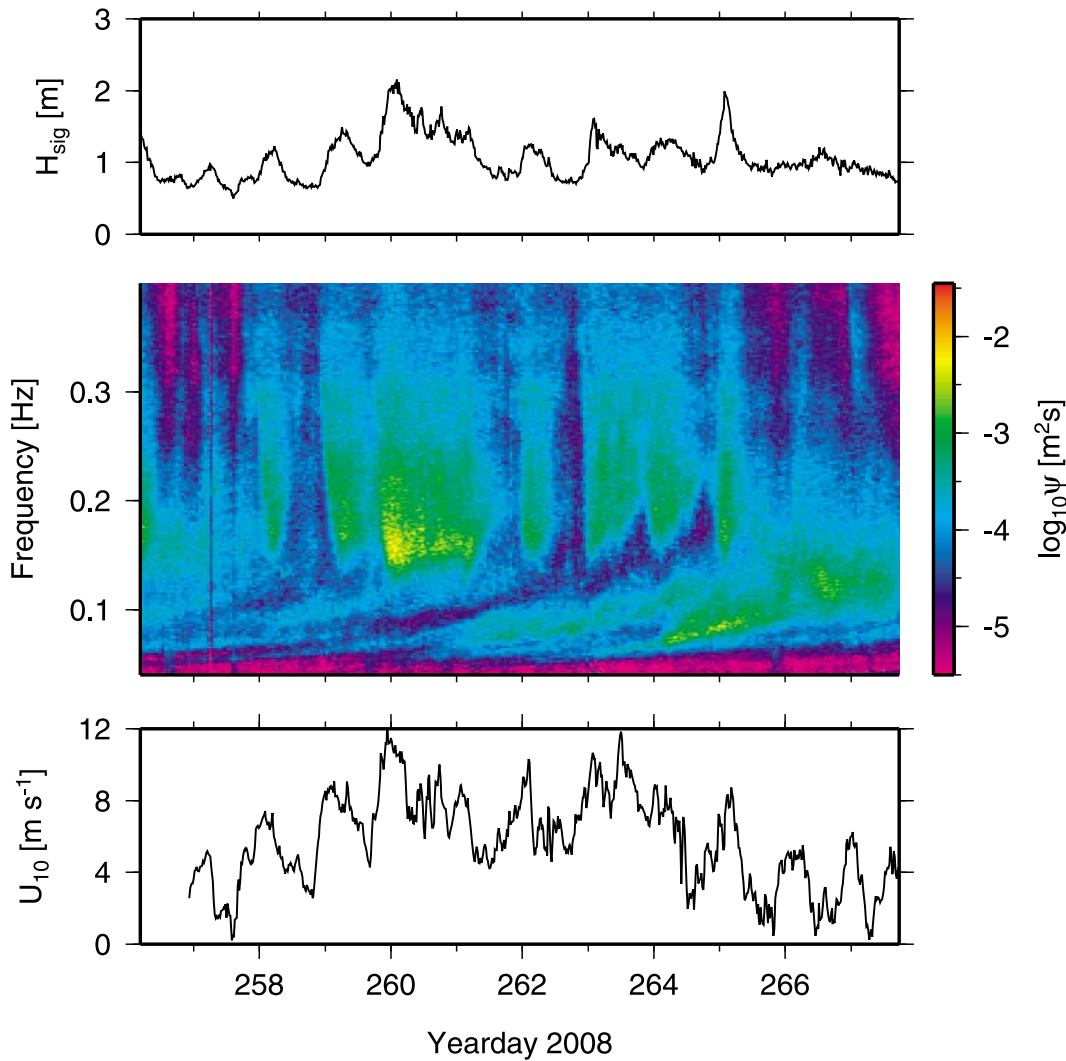
Figure 8. Time series of the significant wave height, H_{sig}, wave height frequency spectrogram, Ψ, and wind speed, U_{10}, during the RaDyO Santa Barbara Channel experiment aboard the R/P *FLIP*. The measurements were made from the starboard boom at a nominal height of 9 m.

4.4. Shape From Polarimetry

[40] The POL camera is an exciting new imaging instrument for detecting very short gravity waves and capillary waves. It produces estimates of the sea surface slope topography of a small patch of the sea surface at high resolution and at video rates.

[41] The phase-resolved, spatial-temporal history of small waves was measured using the shape-from-polarimetry (SFP) technique first described by *Zappa et al.* [2008]. The SFP technique relates the change in polarization of skylight reflecting from water to infer the orientation of the water surface at the point of reflection. The incident skylight strikes the water surface at an angle θ relative to the surface normal. The incident light ray, the surface normal and the reflected light ray form a plane, which intersects the image plane of the polarimeter at an angle, ϕ. The SFP method relates the change in polarization to the incidence angle, and the orientation of the polarization to the tilt of the plane of reflection.

[42] The values of (θ, ϕ) are derived from the Mueller calculus, which relates the polarization state of the incoming and scattered light through a Mueller matrix that depends on the electrical and geometric properties of the scattering media. The polarization state of a bundle of light rays is specified by the Stokes parameters [*Stokes*, 1852]. The Stokes parameters form a four element vector $\mathbf{S} = (S_0, S_1, S_2, S_3)$, where S_0 is the intensity, S_1 and S_2 define the state of linear polarization, and S_3 defines the degree of circular polarization.

[43] The polarization state $\mathbf{S}$ of light reaching a polarimeter looking at a water surface is the sum of the skylight reflected from the water surface $\mathbf{S}_{AW}$ and the light transmitted through the water surface $\mathbf{S}_{WA}$

$$\mathbf{S} = \mathbf{S}_{AW} + \mathbf{S}_{WA}. \qquad (5)$$

The values of $\mathbf{S}_{AW}$ and $\mathbf{S}_{WA}$ are found using Mueller calculus

$$\mathbf{S}_{AW} = \mathbf{R}_{AW} \cdot \mathbf{S}_{SKY} \quad \text{and} \quad \mathbf{S}_{WA} = \mathbf{T}_{WA} \cdot \mathbf{S}_{UP}. \qquad (6)$$
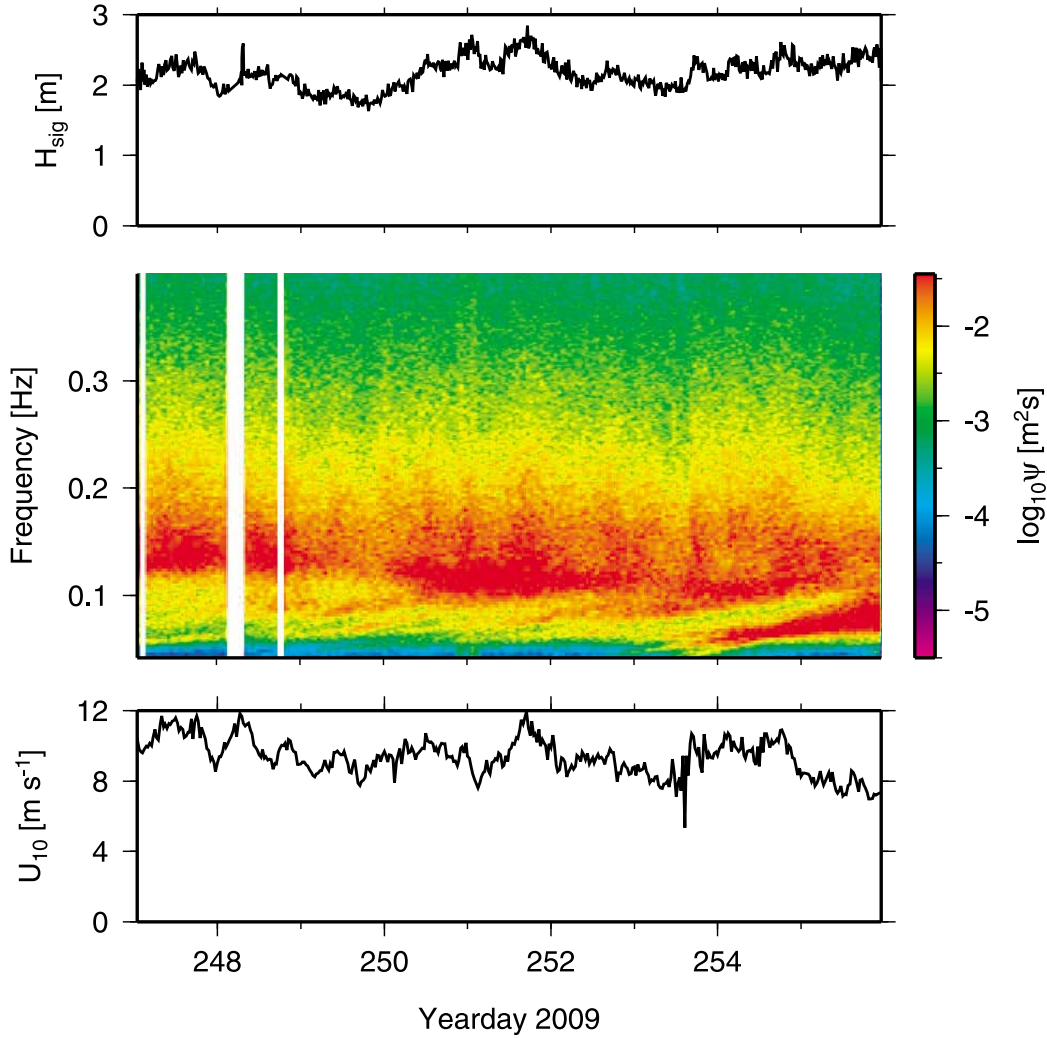
Figure 9. Time series of the significant wave height, H_{sig}, wave height frequency spectrogram, Ψ, and wind speed, U_{10}, during the RaDyO experiment in the central Pacific Ocean south of Hawaii aboard the R/P *FLIP*. The measurements were made from the starboard boom at a nominal height of 9 m.

[44] The Stokes vectors $\mathbf{S}_{\mathrm{SKY}}$ and $\mathbf{S}_{\mathrm{UP}}$ represent downwelling skylight and upwelling light, and $\mathbf{R}_{\mathrm{AW}}$ and $\mathbf{T}_{\mathrm{WA}}$ are the Mueller matrices for reflection and transmission. The explicit forms of the Mueller matrices are

The numbers α, α', η, η', γ_{Re} γ'_{Re} are the Fresnel reflection coefficients [*Kattawar and Adams*, 1989]. The angle θ_i is the incidence angle (the angle between the incidence ray and the surface normal) and the angle θ_t is the transmission angle

$$\mathbf{R}_{\mathrm{AW}} = \begin{bmatrix} \alpha+\eta & \alpha-\eta & 0 & 0 \\ \alpha-\eta & \alpha+\eta & 0 & 0 \\ 0 & 0 & \gamma_{\mathrm{Re}} & 0 \\ 0 & 0 & 0 & \gamma_{\mathrm{Re}} \end{bmatrix} \quad \text{and} \quad \mathbf{T}_{\mathrm{WA}} = \begin{bmatrix} \alpha'+\eta' & \alpha'-\eta' & 0 & 0 \\ \alpha'-\eta' & \alpha'+\eta' & 0 & 0 \\ 0 & 0 & \gamma'_{\mathrm{Re}} & 0 \\ 0 & 0 & 0 & \gamma'_{\mathrm{Re}} \end{bmatrix} .$$

$$\alpha = \frac{1}{2}\left[\frac{\tan(\theta_i-\theta_t)}{\tan(\theta_i+\theta_t)}\right]^2 \quad \eta = \frac{1}{2}\left[\frac{\sin(\theta_i-\theta_t)}{\sin(\theta_i+\theta_t)}\right]^2 \quad \gamma_{\mathrm{Re}} = \frac{\tan(\theta_i-\theta_t)\sin(\theta_i-\theta_t)}{\tan(\theta_i+\theta_t)\sin(\theta_i+\theta_t)}$$

$$\alpha' = \frac{1}{2}\left[\frac{2\sin(\theta'_i)\sin(\theta'_t)}{\sin(\theta'_i+\theta'_t)\cos(\theta'_i+\theta'_t)}\right]^2 \quad \eta' = \frac{1}{2}\left[\frac{2\sin(\theta'_i)\sin(\theta'_t)}{\sin(\theta'_i+\theta'_t)}\right]^2 \quad \gamma'_{\mathrm{Re}} = \frac{4\sin^2(\theta'_t)\sin^2(\theta'_t)}{\sin^2(\theta'_i+\theta'_t)\cos^2(\theta'_i+\theta'_t)}$$
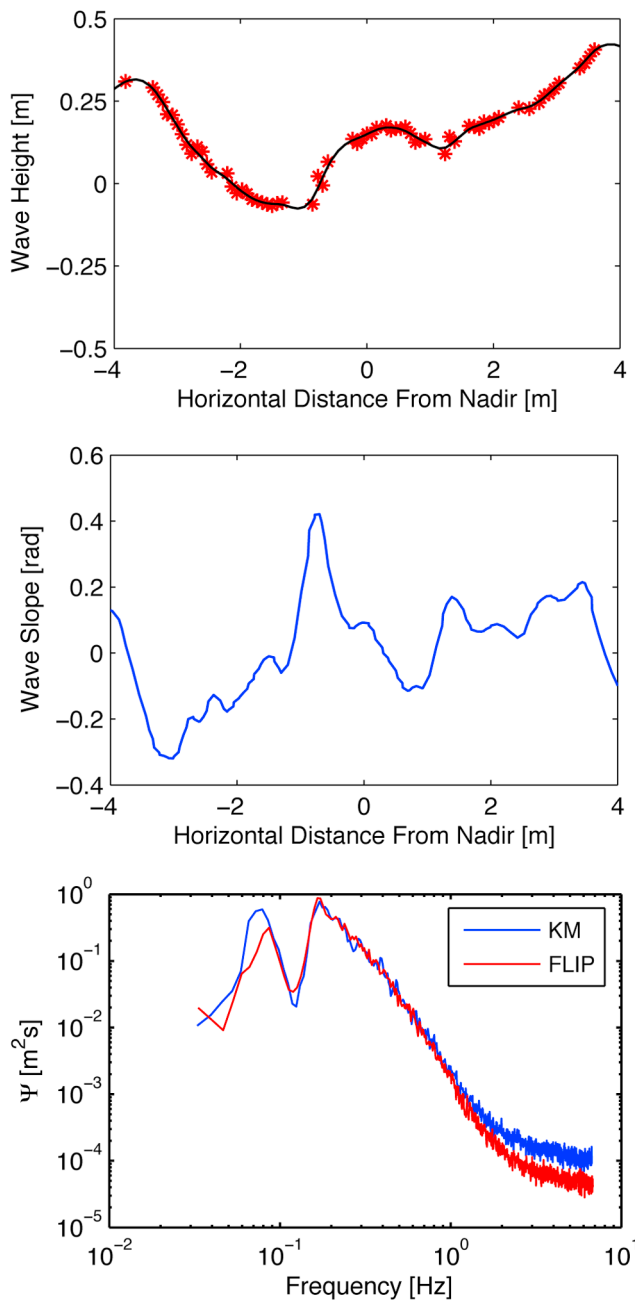
(7)

Figure 10. (top) Example of the measured wave height along an 8 m footprint in the wind direction from the starboard boom on R/P *FLIP*, using a 75 Hz scanning lidar. The red asterisks indicate the lidar data and the black line is the smoothed profile. (middle) Wave slope derived from the smoothed wave height profile in Figure 10 (top). (bottom) A comparison of wave height frequency spectra, Ψ, measured during the same period from R/P *FLIP* and R/V *Kilo Moana*. The wind speed was approximately 10.0 m s^{-1} on yearday 262 2008 in the Santa Barbara Channel.

(the angle between the transmitted ray and the surface normal). The angles θ_i are θ_t are related by Snell's law $\sin(\theta_i) = n \cdot \sin(\theta_t)$ through the index of refraction n. The primes indicate transmission from water to air, in which case the

angles of incidence and transmission are reversed, $\theta'_i = \theta_t$ and $\theta'_t = \theta_i$ and the index of refraction is inverted, $n' = 1/n$.

[45] In general the evaluation of $\mathbf{S}_{AW}$ and $\mathbf{S}_{WA}$ in equation (6) requires knowledge of $\mathbf{S}_{SKY}$ and $\mathbf{S}_{UP}$. For the RaDyO experiments we were able to incorporate three simplifying assumptions that resulted in a closed form solution for θ and ϕ: (1) The skylight is unpolarized, $\mathbf{S}_{SKY} = S_{SKY}(1, 0, 0, 0)$, which is a good assumption for overcast days. (2) In deep, clear water upwelling light can be neglected $\mathbf{S}_{WA} = (0, 0, 0, 0)$. (3) The surface is smooth within the pixel field-of-view, which was approximately 1.5×1.5 mm. Under these conditions, equation (7) leads to a simple relationship for θ and ϕ as a function of the polarization state of the light received by the imaging polarimeter

$$\text{DOLP}(\theta) = \sqrt{\frac{S_1^2 + S_2^2}{S_0^2}} \quad \text{and} \quad \varphi = \frac{1}{2} \tan^{-1}\left(\frac{S_2}{S_1}\right) + 90°. \quad (8)$$

[46] Figure 11 shows the degree of linear polarization (DOLP) as a function of the incidence angle θ, and the sensitivity of DOLP to changes in θ ($\partial \text{DOLP}/\partial \theta$) for an index of refraction of $n = 1.34$. The optimal viewing angle occurs when the sensitivity is at its maximum, approximately 37°.

[47] The SFP method recovers orientation of the surface normal vectors relative to the polarimeter coordinate system. However, in many applications a surface height map in an Earth-based coordinate system is a more desirable product. The orientation of the polarimeter relative to the Earth is found by attaching an inertial measurement unit (IMU) to the polarimeter's case. The x and y components of surface slopes are found by rotating the surface normal vectors to an Earth-based coordinate system.

[48] We have calibrated and processed the Santa Barbara Channel and central Pacific Ocean polarimetric data. This required a significant algorithm development effort, including (1) correcting for fixed pattern noise and (2) correcting for variable gain between sensors. We were able to recover surface slopes with the new POL camera and synchronize
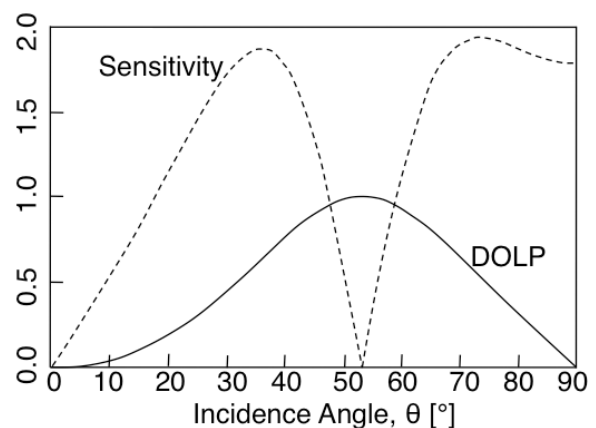

Figure 11. The DOLP as a function of incidence angle θ (solid line) and sensitivity of DOLP to changes in θ (dashed line). The maximum DOLP occurs at Brewster's angle ~53°, and the maximum sensitivity occurs at ~37°.
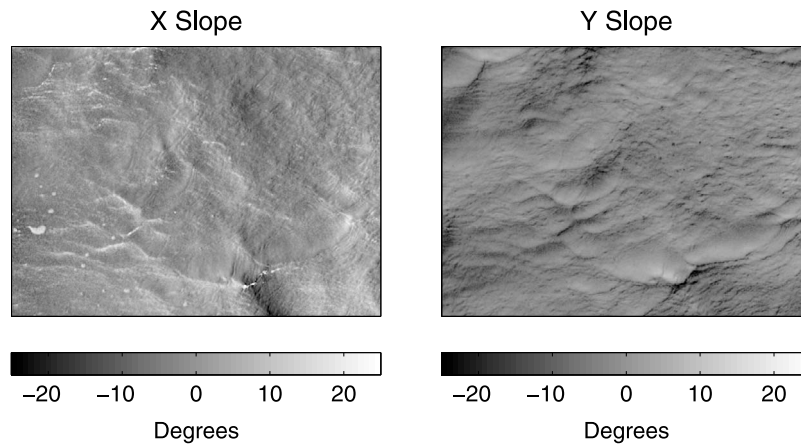
X Slope   **Y Slope**

Figure 12. A typical grayscale image of the (left) X and (right) Y slope slope field of a small patch of sea surface during the Santa Barbara Channel experiment with a wind speed of 9.2 m s^{-1}. A 20 s video time series is available online (Animation 1).

the IR and POL cameras. Figure 12 shows a typical grayscale plot of the x and y components of the surface slope taken during the Santa Barbara Channel field experiment. A 20 s video of the sequence of x and y slope images is available online (Animation 1).[1] The animation shows a wavefield that has capillary waves riding on long- and short-scale gravity waves. These are characterized by steep slopes that also have high spatial variance that exhibits a dimpled structure characteristic of microscale breakers, as observed previously in the laboratory by *Zappa et al.* [2004].

[49] Next, a height map $h(x, y)$ is found by integrating the two-dimensional slope fields ($s_x = \partial h/\partial x$, $s_y = \partial h/\partial y$). Using the integration method outlined by *Frankot and Chellappa* [1988], the Fourier transform of the surface height field is found by evaluating

$$\hat{h}(k_x, k_y) = -i\left(\frac{k_x \hat{s}_x + k_y \hat{s}_y}{k_x^2 + k_y^2}\right), \qquad (9)$$

where the Fourier transform is indicated by ^, $i = \sqrt{-1}$ and (k_x, k_y) are the spatial frequencies in (x, y). The inverse Fourier transform of $\hat{h}(k_x, k_y)$ gives the surface height field $h(x, y)$. This produces a map of the local wave height topography of the imaged patch of the sea surface that is riding on the larger-scale dominant wave. The local mean tilts of the patch are preserved in this processing. Figure 13 shows a shaded relief of a typical reconstructed local surface height topography. A 10 s video of the sequence of reconstructed local surface height topography is available online (Animation 2). Such reconstructions allow investigating for the first time the modulation characteristics of the short wave energy and microscale breaking levels as they ride over the dominant wind sea.

4.5. Polarimeter Slope Validation

[50] The lidar wave height data was used to validate the local wave slope information derived from the colocated polarimeter footprint, as follows. A 1 m baseline was chosen for this task to minimize the errors in the lidar-inferred wave

slope. Figure 14 (top) shows the 1 m baseline wave slope time series derived from the lidar data compared with the 1 m baseline slope time series calculated from the polarimeter data. This representative data was gathered from R/P *FLIP* during 7.5 m s^{-1} winds in the Santa Barbara Channel during September 2008. Figure 14 (bottom left) shows very close agreement between frequency spectra of the 20 min records containing the signals shown in Figure 15 (top). Their high visual correspondence is further confirmed in the coherence spectrum for these data sets shown in Figure 14 (bottom right). This provides a very valuable in situ validation check on the polarimeter performance.

4.6. Mean Squared Slope Dependence on Winds, Currents, and Sea State

[51] The POL camera data were processed to obtain wavenumber-frequency spectra. Figure 15 shows representative wave number-frequency spectra in the wind and crosswind directions. In the wind direction, it is seen that the
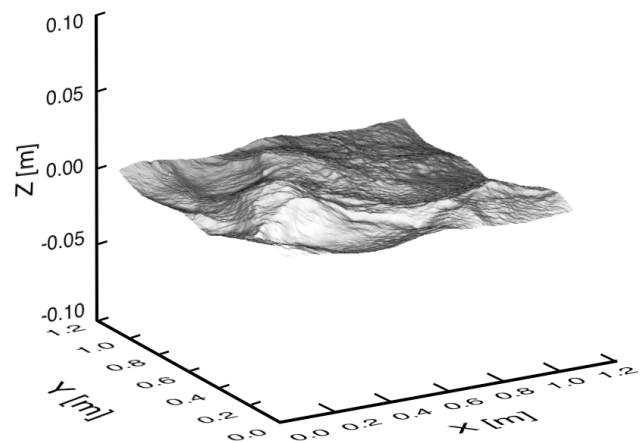
Figure 13. Representative frame from a video sequence showing a reconstructed wave train for the same data shown in Figure 12. The spatial resolution is 1.5 mm, and the temporal resolution is 60 Hz. A 10 s video time series is available online (Animation 2).
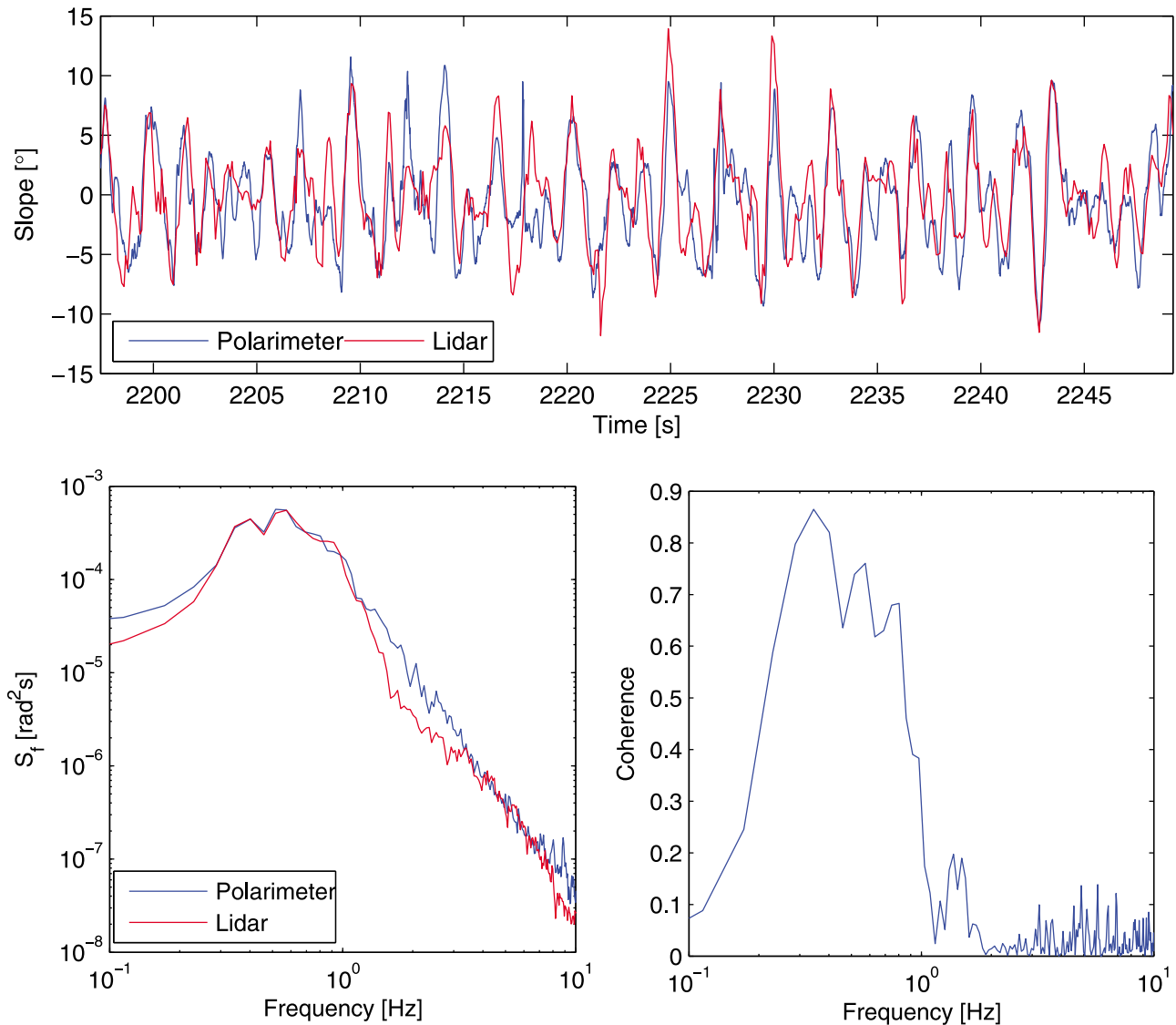
Figure 14. (top) Comparison time series of the local wave slope over a 1 m baseline determined from the polarimeter and scanning lidar instruments; (bottom left) frequency spectra, S_f, of the 20 min records containing the signals shown in Figure 14 (top); and (bottom right) coherence between the slope data sets in Figure 14 (top). These data were taken from R/P *FLIP* with a wind speed of approximately 5.2 m s^{-1} in the Santa Barbara Channel during September 2008.

wave energy follows the deep water dispersion relationship at wave numbers at least up to 100 rad m^{-1} and apparent frequencies up to −40 rad s^{-1} (5 Hz; negative frequencies in our frame of reference implies the waves are traveling toward the viewer; Figure 15, top). At higher wave numbers and frequencies the wave energy spreads but does not depart from the mean dispersion curve for zero-mean current. The main contributing mechanism for this energy spreading is the wave orbital Doppler distortion. We note that wind-drift Doppler-shifting effects can also influence the very high wave number components. The slope energy at a given wave number vector, $\vec{k}$, is Doppler shifted from its intrinsic frequency, ω_o, to its observed mean frequency, ω, by $U_c \cdot \vec{k}$, where U_c is the net surface transport velocity for waves of scale $\vec{k}$. In the absence of along-wind ocean currents, U_c is the wind-drift velocity. Typically, the thin wind drift current

is about 3% of U_{10}, and it advects the very short waves with this velocity. As the wavelength increases, the wind drift influence on propagation decreases, typically vanishing for wavelengths greater than $O(1$ m) at moderate wind speeds. The upper bound of this wind-drift effect is indicated in the along-wind spectrum shown in Figure 15 (top). The wave number-frequency spectrum in the cross-wind direction shows a systematic deviation from the mean dispersion curve for zero-mean current. Here, U_c is the measured cross-wind ocean current of 27.3 cm s^{-1}. This modified dispersion curve for the cross-wind spectrum is shown superimposed in Figure 15 (bottom). It is seen that for wave numbers at least up to 100 rad m^{-1} (Figure 15, bottom), the slope energy conforms to this Doppler modified dispersion relationship.

[52] The total mean square slope (mss) variation with wind speed obtained by processing all the calibrated POL
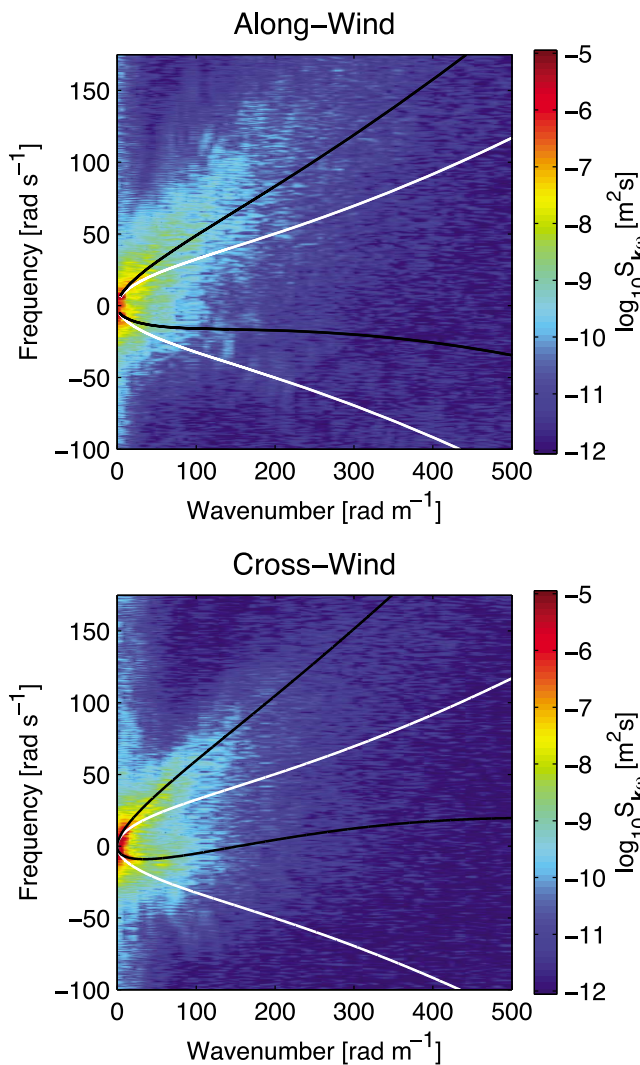
Figure 15. Wave number–frequency spectrum, $S_{k\omega}$, from the polarimeter data in the (top) wind and (bottom) cross-wind directions during the RaDyO Santa Barbara Channel experiment with a wind speed of 5.5 m s^{-1} and an upper ocean current speed, U_c, of 27.3 cm s^{-1} with a relative direction to the wind of 110°. Here, the wind direction and current direction both follow the oceanographic convention of "toward." Positive frequencies are representative of waves propagating in the direction of the forcing. The white trace is the deep water dispersion relationship for ocean waves. The black trace shows that a given wave number vector, $\vec{k}$, is Doppler shifted from its intrinsic frequency, ω_o, to its observed mean frequency, ω, by $U_c \cdot \vec{k}$, where U_c is the net surface transport velocity for waves of scale $\vec{k}$. In the absence of along-wind ocean currents, U_c is the wind-drift velocity (Figure 15, top) and U_c is the measured cross-wind ocean current (Figure 15, bottom).

camera data in both experiments is summarized in Figure 16. Recall that all data has been processed assuming the sky is unpolarized. This figure shows a comparison with the classical sun glint parameterization of *Cox and Munk* [1956] for clean and slick surface conditions. It should be noted that the Santa Barbara Channel is populated by numerous oil

platforms and oil seepage sites that may produce significant spatial and temporal variability in the surfactant concentration. At the SBC site, the sparse spatial and temporal monitoring by *Wurl et al.* [2009] confirmed the presence of low surfactant concentrations in the microlayer and the occasional passage of slicks, though these measurements did not coincide in time with our wave measurements from R/P *FLIP*. Furthermore, even as the weak day-to-day variability in this concentration does not correspond to the variability in our mss observations, we cannot rule out the possible effects of transient slicks. While some of the low mss estimates appear to lie near the Cox-Munk slick parameterization, we surmise that these cases may be attributable to other physical mechanisms. This is explored by close examination of time series of the mss variation compared to the operative environmental conditions shown in Figure 17.

[53] Figure 17 shows time series of the total mss, wind speed, ocean current speed, wind direction relative to the current direction, and the wave height spectrogram for a subset of the Santa Barbara Channel experiment. Here, the wind direction and current direction both follow the oceanographic convention of "toward." These data highlight three interesting episodes of the mss variability designated as I, II, and III. To refine our interpretation of the mss variability, we show the omnidirectional wave number slope spectra from the polarimeter for episodes I, II, and III in Figure 18. Note that the lowest bin of the omnidirectional wave number slope spectra quantifies the mss for all scales longer than the image size. Typically, these scales larger than the image size were found to contribute roughly 20% to the overall mss.
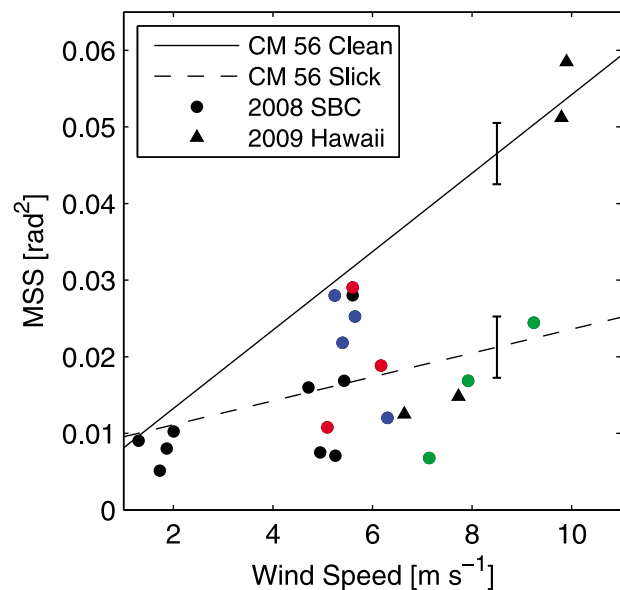

Figure 16. Mean squared total slope against wind speed during the Santa Barbara Channel and Hawaii RaDyO field experiments. The red symbols represent episode I, the blue symbols represent episode II, green symbols represent episode III, and the black symbols represent the rest of the polarimeter data. The solid and dashed lines represent the *Cox and Munk* [1956] best linear fits to their clean surface and slick-covered surface results, respectively. The error bounds to the *Cox and Munk* [1956] best linear fits shown are ±1 standard deviation.

[54] For the first group (episode I), while the mss doubles over this episode, the wind speed increases only slightly from 4.6 to 6.5 m s^{-1} and the dominant wind sea does not change as observed from the wave height frequency spectrum. We attribute the increase in mss primarily to the response of the small-scale gravity-capillary waves to the modest increase in wind speed. This increase in the surface roughness is due to the broadbanded increase in the wave slope spectral energy shown in Figure 18a from 7 to 1500 rad m^{-1}, as determined from the high-resolution POL imagery. The contribution to the mean square slope increase for wave numbers between 100 and 1000 rad m^{-1} is greater than lower wave numbers for the early half of episode I. During the latter half of episode I, wave numbers less than 100 rad m^{-1} contribute more to the mean square slope increase. The currents are noted to increase from 8.7 to 19 cm s^{-1} with a direction that shifts from 50° to 95° relative to the wind.

[55] For the second group (episode II), the mss halved over this episode, even though the wind speed increases from 5.2 to 7.1 m s^{-1}. During this episode, the dominant wind sea decreased as observed from the wave height frequency spectra and the spectral level is nearly halved over the range of 0.1 to 3.0 Hz. The omnidirectional wave number slope spectra in Figure 18b from the polarimeter also show a marked broadbanded decrease in the slope spectral energy from 7 to 1500 rad m^{-1}. During the first half of episode II, the contribution of the high wave numbers between 100 and 1000 rad m^{-1} to the decrease in mss is larger than for lower wave numbers. During the latter half of episode II, wave numbers below 100 rad m^{-1} dominate the decrease in mss. Thus, for this episode, the small-scale gravity-capillary waves contribute to the decrease in mss. The currents are noted to vary between 18 and 26 cm s^{-1} with a direction that meanders slowly at 90° ± 20° relative to the wind (with a 20° turn above and below 90°).

[56] For the third group (episode III), the mss halves over this episode as the wind speed decreases from 9.5 to 7.3 m s^{-1}. The peak in the dominant wind sea downshifted from 0.25 to 0.20 Hz over 7 h with an increase of 10% in wave energy, and the high-frequency energy increased by 10% in the bandwidth of 1 to 8 Hz. The currents are noted to increase from 6.4 to 20.5 cm s^{-1} with a direction that is roughly −45° to −70° relative to the wind. The omnidirectional wave number slope spectra in Figure 18c from the polarimeter show a marked decrease in the slope spectral energy out to 800 rad m^{-1} during the first half of the episode III, dominated by the gravity wave components longer than 1 m. Subsequently, the decrease in slope spectral energy was dominated by scales between 7 and 300 rad m^{-1}. Even though a modest increase in the dominant wind sea energy occurs, we attribute the decrease in mss primarily to the response of the small-scale gravity-capillary waves to the decrease in wind speed and the increasing current approximately in the direction of the wind. Coflowing wind and current tends to reduce the input forcing to the waves, especially for the slower-moving short components, and consequently a reduction in their slope.

[57] *Zhang et al.* [2009] suggested that the vertical vorticity component, $\Omega = dU_c/dy - dV_c/dx$, is the most appropriate measure of the horizontal shear and that the horizontal shear is an important factor in modifying the wind stress direction relative to the wind direction. Here dU_c/dy and dV_c/dx are the surface horizontal shear components. We investigated this hypothesis in seeking to explain the variability observed for the highlighted episodes I, II, and III. Horizontal shear information at 1 km resolution was available using the surface currents from the HF radar data. The observed Ω within a 2 km box centered on R/P *FLIP* in episode 1 is 0.15f. The wind stress in episode I was typically shifted by 30° from the wind direction, the very low horizontal shear suggests this mechanism was not operative. In episode II, Ω is 0.65f in the beginning and decreases to 0.15f. However, the wind direction and the wind stress direction were nearly coincident (within ±5°) suggesting that horizontal shear is not playing a major role. For episode III, Ω fluctuates between −0.01f and −0.73f with a mean value of −0.29f ± 0.23f. The steering of the wind stress in episode III was rather small (±5°) despite the highly variable but small relative vorticity. Hence, based on these three episodes, we do not observe any compelling evidence linking the horizontal shear to the steering of the wind stress.

[58] *Kudryavtsev et al.* [1997] investigated systematic short wave variations through coupled modulation by long waves and wind stress. According to their model results, at the relatively low wind speeds typical of our observations, the modulation is dominated by hydrodynamic straining of the short waves by the long waves. During episode I, modulation associated with the wind sea may have contributed to the observed variation of the mss, but the relative importance of the modulational contribution is not known from the data alone. For episode II, despite the observed decrease in mss, the extremely low steepness wind sea suggests that modulational effects may not be important in influencing the mss variation. For episode III, the coflowing wind and current effect described above appears to dominate any modulational influence.

[59] In summary, these observations highlight the possible oversimplification of the classic Cox-Munk view that mss increases linearly with wind speed. They also suggest the potential importance of upper ocean currents and modulation of the short waves by longer waves in addition to the wind. These results are timely considering issues raised in the recent review article on the conundrums of capillary-gravity waves [*Munk*, 2009].

4.7. Breaking Crest Length Distributions

[60] The polarimeter provides high-resolution information on the sea surface roughness for unbroken surfaces including the probability density function of the slopes. Breaking waves provide another mechanism for influencing the optical path at the air-sea interface. There is a need to better quantify the statistical properties of breakers with respect to scale in order to improve the accuracy of radiative transfer models.

[61] *Phillips* [1985] proposed a spectral framework for breaking waves and their dynamics. In this context, the key measure for quantifying remotely sensed wave breaking imagery is the spectral density of breaking crest length per unit area, $\Lambda(c_b, \theta)$, where c_b, θ are the breaker crest speed and crest propagation direction, respectively. The mean total length of breaking crests per unit area is then
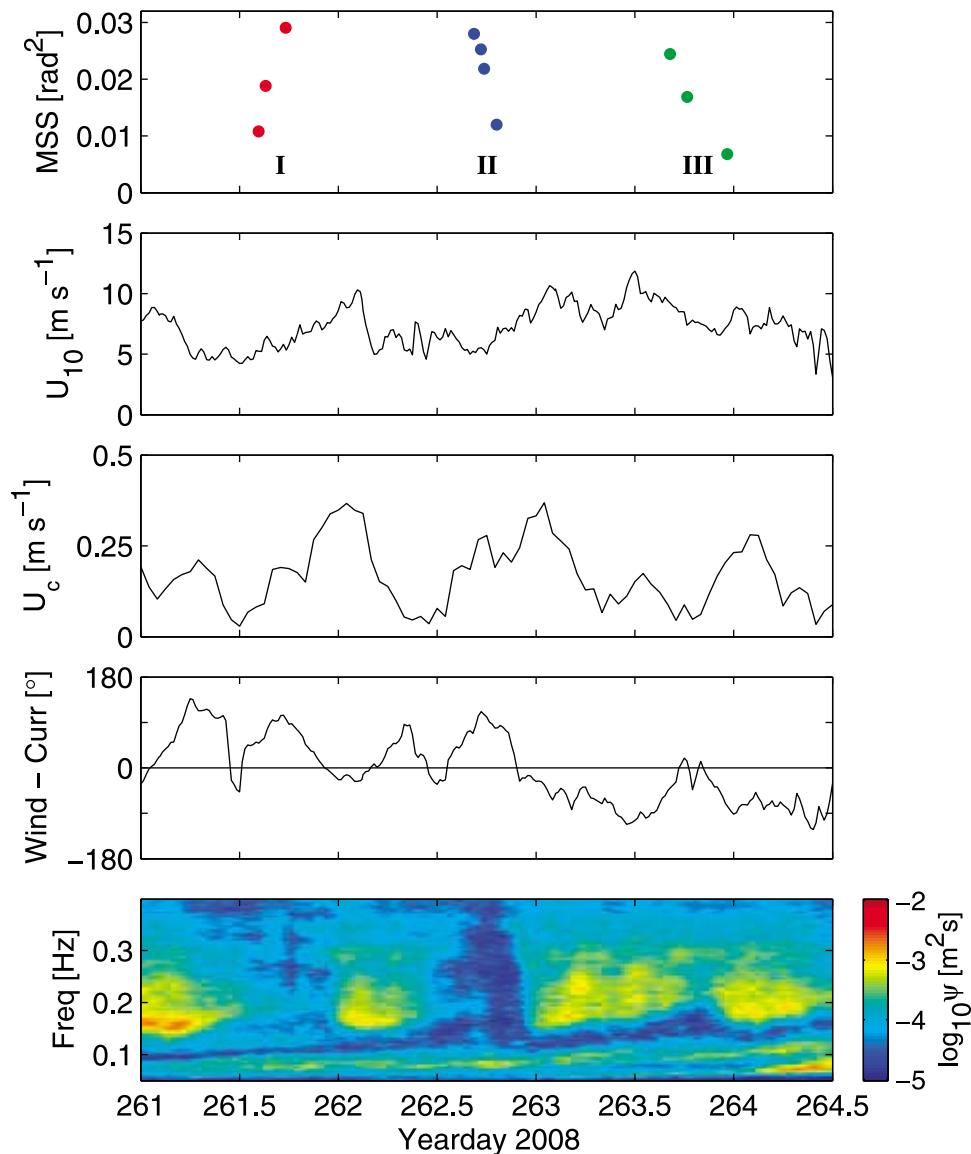
Figure 17. Time series of the total mean square slope (mss), wind speed, ocean current speed, wind direction relative to the current direction, and the wave height spectrogram for a subset of the Santa Barbara Channel experiment. Here the wind direction and current direction both follow the oceanographic convention of "toward." The color code identifying episodes I, II, and III is the same as in Figure 16.

$L = \int \Lambda(c_b, \theta)dc_b \, d\theta$. Also, various moments of Λ can be used to estimate a number of key air-sea interfacial properties, including swept whitecap area with respect to scale, whitecap cover and the upper ocean dissipation rate.

[62] Thus, by definition, $\Lambda(c_b,\theta)$ is the distribution of total breaking crest lengths per unit area as a function of breaker speed and direction, which can be extracted readily from video or infrared imagery. Subsequent to *Phillips* [1985] proposing his framework, it was noted in laboratory studies that the breakers travel measurably more slowly than the corresponding unbroken waves from which they evolve [e.g., *Rapp and Melville*, 1990, Figure 33; *Stansell and MacFarlane*, 2002, Figure 5]. Thus, it was proposed that $c_b = \alpha c$, where α was estimated to lie in the range 0.7 to 0.9 in these laboratory studies of idealized 2-D wave packets.

Notwithstanding this complication, the Λ distribution is emerging as a useful spectral description of wave-breaking kinematics, and has potential extension to wave-breaking dynamics. Several recent video observations from ships, aircraft and towers have measured Λ distributions during various sea states [e.g., *Gemmrich et al.*, 2008; *Kleiss and Melville*, 2010; *Melville and Matusov*, 2002; *Mironov and Dulov*, 2008; *Thomson et al.*, 2009]. To be able to relate the breaking kinematics to the dynamics, a breaking strength coefficient ('b') needs to be determined [*Phillips*, 1985, equation 6.3], which is presently the subject of ongoing investigation within our RaDyO effort.

[63] We measured $\Lambda(c_b)$ during both the Santa Barbara Channel and the Hawaii experiments with our suite of video and infrared cameras mounted on R/P *FLIP*. The scale of wave breaking during both field experiments ranged from
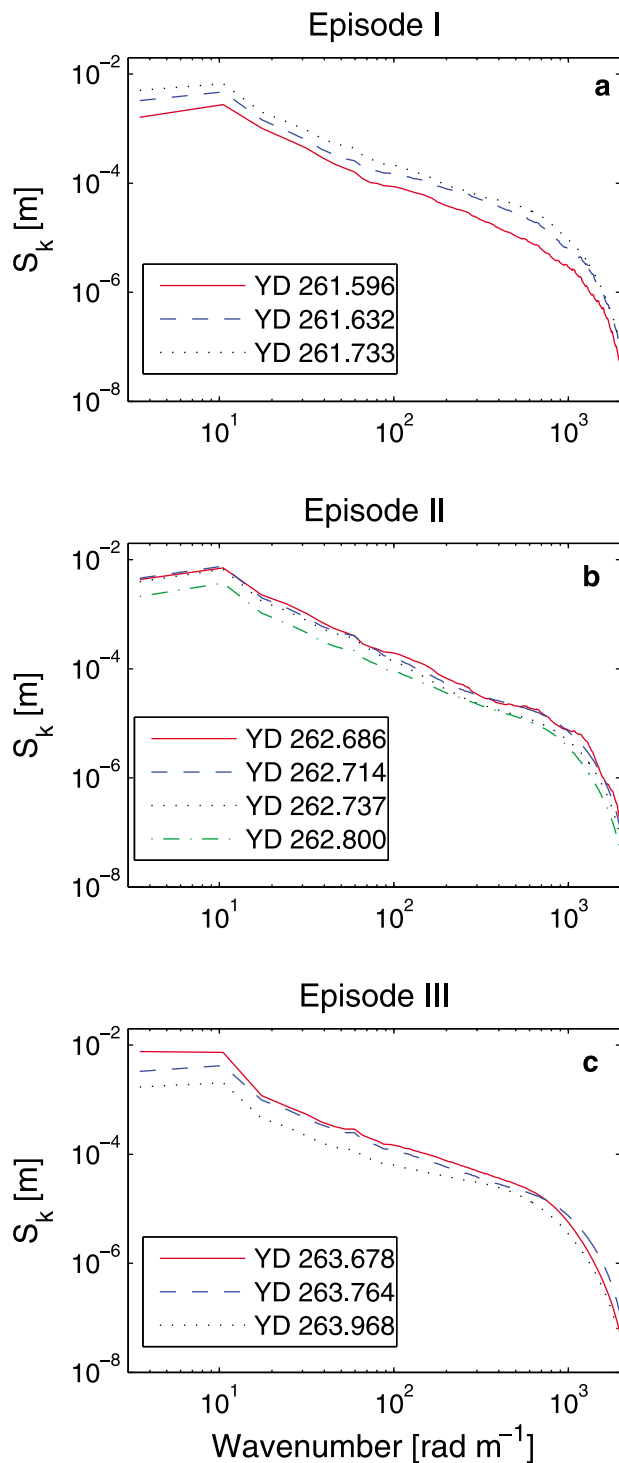
Figure 18. Omnidirectional wave number spectra for (a) episode I, (b) episode II, and (c) episode III shown in Figure 17. The yearday is indicated to highlight the progression of runs within an episode.

microbreakers to small-scale breakers with air entrainment to breaking dominant waves. These data were analyzed in terms of breaking crest length density, foam coverage and whitecap persistence. Results on the breaking crest length distribution $\Lambda(c_b)$ independent of direction, obtained from visible imagery using the discrete breaker tracking decomposition

method, are shown in Figure 19 (left) for RaDyO experiments in Santa Barbara Channel and in Figure 19 (right) for the central Pacific Ocean south of Hawaii. Comparison of $\Lambda(c_b)$ determined from our visible and infrared imagery at a similar wind speed of 10 m s^{-1} shows that the infrared captures the microbreaking at smaller breaking scales, confirming that these roughness features are important to the breaking distribution.

[64] From the ensemble of $\Lambda(c_b)$ in Figure 19, a primary observation is that the overall mean level of $\Lambda(c_b)$ is larger in the central Pacific Ocean south of Hawaii than in Santa Barbara Channel, even though the mean wave age was considerably older. Also, for longer waves, the slope of the family of $\Lambda(c_b)$ curves is close to the *Phillips* [1985] canonical form $\Lambda(c_b) \sim c_b^{-6}$ for the Santa Barbara Channel and tends to be marginally steeper for the Hawaii experiment. Last, the dynamic range of the individual $\Lambda(c_b)$ distributions is much higher in the Santa Barbara Channel, fluctuating by more than an order of magnitude. This behavior is primarily associated with the much larger synoptic variations of the wind stress in SBC (see Figure 6). This also results in a larger dynamic range of wave age in the SBC experiment compared to the Hawaii experiment.

[65] Upon closer inspection, the slopes of the individual distributions are noticeably different both within and between experiments. The levels of $\Lambda(c_b)$ at larger scales in both the SBC and Hawaii experiments are comparable. However, the level of $\Lambda(c_b)$ at intermediate scales is higher in Hawaii compared to SBC. This suggests that intermediate breaking scales are more important in Hawaii, while the relative contribution of larger-scale breakers during the Santa Barbara Channel experiment is stronger.

[66] Further features of interest are evident. It is seen that $\Lambda(c_b)$ for small-scale wave breaking was significantly less in the central Pacific Ocean south of Hawaii than in Santa Barbara Channel. For both experiments, the maximum of $\Lambda(c_b)$ is seen to occur in the short gravity wave range with the maximum for the SBC experiment occurring at slightly shorter scales compared to Hawaii. The peak levels of $\Lambda(c_b)$ for each experiment are comparable.

[67] We had anticipated that the mean $\Lambda(c_b)$ levels would be higher for younger seas. The data set from the Santa Barbara Channel provided a range of wave ages to investigate this hypothesis. The highest levels of $\Lambda(c_b)$ occur at intermediate wave ages, when the wavefield is well developed but also subject to significant wind stress. Older seas correspond to declining wind forcing which quickly results in reduced wave breaking, whereas the youngest seas showed active breaking but mainly at small wave scales.

[68] While the wave age effects did conform to the anticipated perspective, the overall $\Lambda(c_b)$ levels in SBC were lower compared to Hawaii. To gain a better understanding of the differences in $\Lambda(c_b)$ between SBC and Hawaii, an investigation of the role of complex surface currents that characterize the Santa Barbara Channel known from the HF radar current maps appeared to be relevant. Our initial survey of the role of currents in the SBC data indicated that the overall level of $\Lambda(c_b)$ appeared to be affected by the complex structure of surface currents in the channel. For example, the increase in wind and current just following episode I at yearday 262 (see Figure 17) resulted in an increase of the mean $\Lambda(c_b)$ level at intermediate scales whereas during
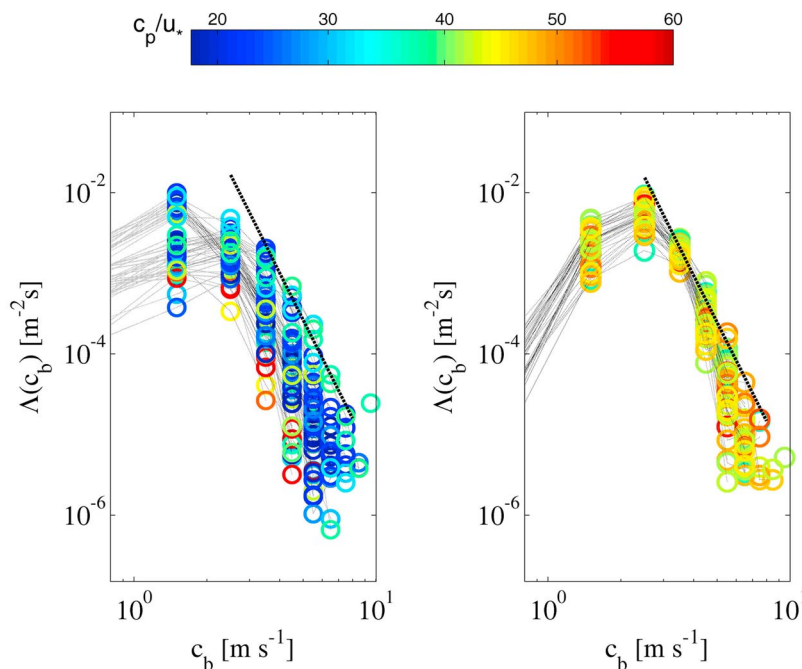
Figure 19. Breaking crest length distributions during the (left) Santa Barbara Channel and (right) Hawaii experiments. Note that the wave age (c_p/u_*) shows young wind seas in the Santa Barbara Channel compared to old wind seas south of Hawaii. The dashed line represents the c^{-6} dependence predicted by *Phillips* [1985].

episode II (i.e., yearday 263.8) with a similar increase in wind speed and currents, the mean $\Lambda(c_b)$ level decreased to a level 70% lower. It is interesting to note that during episode I, a sharp increase in mss preceded the increase in $\Lambda(c_b)$, consistent with a rapidly growing wind sea. Also we observed that during episode II, a strong decrease in $\Lambda(c_b)$ coincided a sharp decrease in mss. The major difference between the two episodes is the direction of the current relative to the wind. For episode I, the current was predominantly along wind while for episode II the current was predominantly cross wind. Thus from our initial study, the key issue of the overall lower mean level of $\Lambda(c_b)$ in the SBC compared with Hawaii appears linked to the complex currents operative in the SBC, and further analysis is warranted to gain a better understanding of this fundamental process of wind-current-breaking wave interaction.

[69] Further, a clear robust transition to a different c_b dependence occurs for very short gravity waves and below. The underlying dynamics producing the maximization if $\Lambda(c_b)$ is not known and will be a focus of continued investigation of the RaDyO data. Regardless, we observe that $\Lambda(c_b)$ for whitecapping is reduced significantly and departs from the c_b^{-6} dependence observed for longer waves. This behavior also appears in previous data sets using visible imagery [*Gemmrich et al.*, 2008; *Kleiss and Melville*, 2010; *Thomson et al.*, 2009]. However, the visibility of whitecaps declines at shorter scales due to reduced air entrainment producing a reduction in the observed $\Lambda(c_b)$. In these situations, breaking is still ongoing but without air entrainment, i.e., microbreaking, and will contribute to $\Lambda(c_b)$. In RaDyO, we are investigating whether the improved capability to quantify microbreaking using IR imagery can provide more

accurate estimates of $\Lambda(c_b)$ at these shorter scales. A detailed discussion of the wave breaking kinematics and dynamics based on these distributions, as well as the extension of the breaking crest length distributions to include microscale breakers without visible air entrainment, will follow in a subsequent publication.

5. Conclusions

[70] The RaDyO program sought to refine present understanding of light transmission through the wind driven sea surface into the upper ocean, of which a key component is a more complete characterization of the sea surface roughness. Two intensive field experiments from RP *FLIP* were staged within the ONR's RaDyO field program in the Santa Barbara Channel and central Pacific Ocean south of Hawaii. Both established and novel measurement methodologies were deployed to increase present knowledge of sea surface roughness, especially at the microscale. This paper describes (1) the ensemble of instrumentation deployed to address this goal, (2) a detailed documentation of the ambient environmental conditions that prevailed during the RaDyO field experiments, and (3) highlights of exciting new sea surface roughness measurement capabilities.

[71] The two field sites were chosen to provide different sea state conditions – sheltered with moderate winds and sea states (Santa Barbara Channel) and open ocean with higher winds and sea states (central Pacific Ocean south of Hawaii). The Santa Barbara Channel conditions were characterized by (1) low to moderate westerly wind speeds with a strong diurnal cycle and (2) complicated wind and swell wave conditions with a wind sea that also showed a diurnal cycle

and an average significant wave height of 1.1 ± 0.3 m. The conditions in the central Pacific Ocean south of Hawaii were characterized by (1) moderate easterly wind speeds that decreased slowly during the experiment and (2) a steady wavefield with higher overall peak wave energy compared to Santa Barbara Channel and a significant wave height that averaged 2.2 ± 0.2 m.

[72] Our observations during the RaDyO experiments are consistent with the measurements reported by *Edson* [2008] from similar fixed or stable platforms such as R/P *FLIP*. The TOGA-COARE 3.0 model prediction overestimates the measured latent heat flux for SBC and for the Pacific Ocean south of Hawaii. *Edson* [2008] has suggested the need to update the model transfer coefficients including a reduction in the Dalton number by up to 25% for winds below 10 m s^{-1}. Thus, our measurements would be within 5% of the new TOGA-COARE model estimates.

[73] The observations gathered comprised standard marine environmental variables (winds, waves and fluxes). Our roughness measurements were highlighted by the first field deployment of our polarimeter for detecting wavefields down to 1.5 mm wavelengths at sample rates up to 60 Hz. These high-resolution measurements were complemented by colocated scanning and fixed lidars. In addition, colocated video and infrared imagery gave an unprecedented coverage of the sea surface microstructure including breaking waves, over a range of wind speeds and underlying sea states. This paper highlights the experimental conditions and typical data products derived successfully during our RaDyO study.

[74] For instance, a new polarimetric imaging camera highlights the complex interplay of processes in shaping the roughness of the sea surface. These small-scale slope observations by polarimetry highlight the possible over-simplification of the classic Cox-Munk view that mss increases linearly with wind speed. They suggest the potential importance of upper ocean currents in addition to the wind. These results are timely considering issues raised in the recent review article on the conundrums of capillary-gravity waves [*Munk*, 2009].

[75] In addition, the breaking crest length spectral density derived from visible and infrared imagery is shown to be modulated by the development of the wavefield (wave age) and alignment of the wind and surface currents at the inter-mediate (dominant) scale of wave breaking. A primary observation is that the overall mean level of $\Lambda(c_b)$ is larger in the central Pacific Ocean south of Hawaii than in Santa Barbara Channel, even though the mean wave age was considerably older. While the wave age effects did conform to the anticipated perspective within each RaDyO experi-ment, the overall lower mean level of $\Lambda(c_b)$ in the SBC compared with Hawaii appears linked to the complex cur-rents operative in the SBC. Further analysis is warranted to gain a better understanding of this fundamental process of wind-current-breaking wave interaction.

References

Banner, M. L., and D. H. Peregrine (1993), Wave breaking in deep water, *Annu. Rev. Fluid Mech.*, *25*, 373–397, doi:10.1146/annurev.fl.25. 010193.002105.

Businger, J. A., and A. C. Delaney (1990), Chemical sensor resolution required for measuring surface fluxes by three common micrometeorological techniques, *J. Atmos. Chem.*, *10*, 399–410, doi:10.1007/BF00115782.

Cox, C., and W. Munk (1954a), Measurement of the roughness of the sea surface from photographs of the sun's glitter, *J. Opt. Soc. Am.*, *44*(11), 838–850, doi:10.1364/JOSA.44.000838.

Cox, C., and W. Munk (1954b), Statistics of the sea surface derived from sun glitter, *J. Mar. Res.*, *13*(2), 198–227.

Cox, C., and W. Munk (1956), Slopes of the sea surface deduced from photographs of sun glitter, *Bull. Scripps Inst. Oceanogr.*, *6*(9), 401–487.

Dorman, C. E., and D. Koračin (2008), Response of the summer marine layer flow to an extreme California coastal bend, *Mon. Weather Rev.*, *136*, 2894–2992, doi:10.1175/2007MWR2336.1.

Dorman, C. E., and C. D. Winant (1995), Buoy observations of the atmo-sphere along the west coast of the United States, 1981–1990, *J. Geophys. Res.*, *100*, 16,029–16,044.

Dorman, C. E., and C. D. Winant (2000), The structure and variability of the marine atmosphere around the Santa Barbara Channel, *Mon. Weather Rev.*, *128*, 261–282, doi:10.1175/1520-0493(2000)128<0261:TSAVOT> 2.0.CO;2.

Downing, H. D., and D. Williams (1975), Optical constants of water in the infrared, *J. Geophys. Res.*, *80*(12), 1656–1661, doi:10.1029/ JC080i012p01656.

Drennan, W. M., K. K. Kahma, and M. A. Donelan (1999), On momentum flux and velocity spectra over waves, *Boundary Layer Meteorol.*, *92*, 489–515, doi:10.1023/A:1002054820455.

Dupuis, H., P. K. Taylor, A. Weill, and K. Katsaros (1997), Inertial dissipa-tion method applied to derive turbulent fluxes over the ocean during the Surface of the Ocean, Fluxes and Interactions with the Atmosphere/ Atlantic Stratocumulus Transition Experiment (SOFIA/ASTEX) and Structure des Echanges Mer-Atmosphère, Propriétés des Hétérogénéités Océaniques: Recherche Experimentale (SEMAPHORE) experiments with low to moderate wind speeds, *J. Geophys. Res.*, *102*(C9), 21,115–21,129, doi:10.1029/97JC00446.

Edson, J. B. (2008), Review of air-sea transfer processes, in *Proceedings of the ECMWF Workshop on Ocean-Atmosphere Interactions: 10–12 November 2008*, pp. 7–25, Eur. Cent. for Medium Range Forecasts, Reading, U. K.

Edson, J. B., A. A. Hinton, K. E. Prada, J. E. Hare, and C. W. Fairall (1998), Direct covariance flux estimates from mobile platforms at sea, *J. Atmos. Oceanic Technol.*, *15*(2), 547–562, doi:10.1175/1520-0426(1998) 015<0547:DCFEFM>2.0.CO;2.

Fairall, C. W., E. F. Bradley, J. E. Hare, A. A. Grachev, and J. B. Edson (2003), Bulk parameterization of air-sea fluxes: Updates and verification for the COARE algorithm, *J. Clim.*, *16*, 571–591, doi:10.1175/1520-0442(2003)016<0571:BPOASF>2.0.CO;2.

Frankot, R. T., and R. Chellappa (1988), A method for enforcing integrability in shape from shading algorithms, *IEEE Trans. Pattern Anal. Mach. Intell.*, *10*(4), 439–451, doi:10.1109/34.3909.

Gemmrich, J. R., M. L. Banner, and C. Garrett (2008), Spectrally resolved energy dissipation and momentum flux of breaking waves, *J. Phys. Ocea-nogr.*, *38*, 1296–1312, doi:10.1175/2007JPO3762.1.

Hara, T., E. J. Bock, J. B. Edson, and W. R. McGillis (1998), Observation of short wind waves in coastal waters, *J. Phys. Oceanogr.*, *28*(7), 1425–1438, doi:10.1175/1520-0485(1998)028<1425:OOSWWI>2.0.CO;2.

Hara, T., K. A. Hanson, E. J. Bock, and B. M. Uz (2003), Observation of hydrodynamic modulation of gravity-capillary waves by dominant gravity waves, *J. Geophys. Res.*, *108*(C2), 3028, doi:10.1029/2001JC001100.

Hellerman, S., and M. Rosenstein (1983), Normal monthly wind stress over the world ocean with error estimates, *J. Phys. Oceanogr.*, *13*, 1093–1104, doi:10.1175/1520-0485(1983)013<1093:NMWSOT>2.0.CO;2.

Holthuijsen, L. H., and T. H. C. Herbers (1986), Statistics of breaking waves observed as whitecaps in the open sea, *J. Phys. Oceanogr.*, *16*, 290–297, doi:10.1175/1520-0485(1986)016<0290:SOBWOA>2.0.CO;2.

Jessup, A. T., and K. R. Phadnis (2005), Measurement of the geometric and kinematic properties of microscale breaking waves from infrared imagery using a PIV algorithm, *Meas. Sci. Technol.*, *16*, 1961–1969, doi:10.1088/0957-0233/16/10/011.

Kattawar, G. W., and C. N. Adams (1989), Stokes vector calculations of the submarine light field in an atmosphere-ocean with scattering according to a Rayleigh phase matrix: Effect of interface refractive index on radiance and polarization, *Limnol. Oceanogr.*, *34*(8), 1453–1472, doi:10.4319/lo.1989.34.8.1453.

Kleiss, J. M., and W. K. Melville (2010), Observations of wave breaking kinematics in fetch-limited seas, *J. Phys. Oceanogr.*, *40*, 2575–2604, doi:10.1175/2010JPO4383.1.

Kudryavtsev, V. N., C. Mastenbroek, and V. K. Makin (1997), Modulation of wind ripples by long surface waves via the air flow: A feedback mechanism, *Boundary Layer Meteorol.*, *83*, 99–116, doi:10.1023/A:1000278225089.

Melville, W. K. (1996), The role of surface-wave breaking in air-sea interaction, *Annu. Rev. Fluid Mech.*, *28*, 279–321, doi:10.1146/annurev.fl.28.010196.001431.

Melville, W. K., and P. Matusov (2002), Distribution of breaking waves at the ocean surface, *Nature*, *417*, 58–63, doi:10.1038/417058a.

Mironov, A. S., and V. A. Dulov (2008), Detection of wave breaking using sea surface video records, *Meas. Sci. Technol.*, *19*, 015405, doi:10.1088/0957-0233/19/1/015405.

Mobley, C. D. (1994), *Light and Water: Radiative Transfer in Natural Waters*, 592 pp., Academic, San Diego, Calif.

Munk, W. H. (1950), On the wind-driven ocean circulation, *J. Meteorol.*, *7*(2), 80–93, doi:10.1175/1520-0469(1950)007<0080:OTWDOC>2.0.CO;2.

Munk, W. (2009), An inconvenient sea truth: Spread, steepness, and skewness of surface slopes, *Annu. Rev. Mar. Sci.*, *1*, 377–415, doi:10.1146/annurev.marine.010908.163940.

Payne, R. E. (1972), Albedo of the sea surface, *J. Atmos. Sci.*, *29*, 959–970, doi:10.1175/1520-0469(1972)029<0959:AOTSS>2.0.CO;2.

Phillips, O. M. (1985), Spectral and statistical properties of the equilibrium range in wind-generated gravity waves, *J. Fluid Mech.*, *156*, 505–531, doi:10.1017/S0022112085002221.

Phillips, O. M., F. L. Posner, and J. P. Hanson (2001), High resolution radar measurements of the speed distribution of breaking events in wind-generated ocean waves: Surface impulse and wave energy dissipation rates, *J. Phys. Oceanogr.*, *31*, 450–460, doi:10.1175/1520-0485(2001)031<0450:HRRRMO>2.0.CO;2.

Rapp, R. J., and W. K. Melville (1990), Laboratory measurements of deep-water breaking waves, *Philos. Trans. R. Soc. London, Ser. A*, *331*(1622), 735–800, doi:10.1098/rsta.1990.0098.

Skyllingstad, E. D., P. Barbour, and C. E. Dorman (2001), The dynamics of northwest summer winds over the Santa Barbara Channel, *Mon. Weather Rev.*, *129*, 1042–1061, doi:10.1175/1520-0493(2001)129<1042:TDONSW>2.0.CO;2.

Stansell, P., and C. MacFarlane (2002), Experimental investigation of wave breaking criteria based on wave phase speeds, *J. Phys. Oceanogr.*, *32*(5), 1269–1283, doi:10.1175/1520-0485(2002)032<1269:EIOWBC>2.0.CO;2.

Stokes, G. G. (1852), On the composition and resolution of streams of polarized light from different sources, *Trans. Cambridge Phil. Soc.*, *9*, 399–416.

Thomson, J., J. R. Gemmrich, and A. T. Jessup (2009), Energy dissipation and the spectral distribution of whitecaps, *Geophys. Res. Lett.*, *36*, L11601, doi:10.1029/2009GL038201.

Winant, C. D., and C. E. Dorman (1997), Seasonal patterns of surface wind stress and heat flux over the Southern California Bight, *J. Geophys. Res.*, *102*, 5641–5653, doi:10.1029/96JC02801.

Wurl, O., L. Miller, R. Röttgers, and S. Vagle (2009), The distribution and fate of surface-active substances in the sea-surface microlayer and water column, *Mar. Chem.*, *115*, 1–9, doi:10.1016/j.marchem.2009.04.007.

Wyrtki, K. (1974), Equatorial currents in the Pacific 1950 to 1970 and their relation to winds, *J. Phys. Oceanogr.*, *4*, 372–380, doi:10.1175/1520-0485(1974)004<0372:ECITPT>2.0.CO;2.

Wyrtki, K., and G. Meyers (1976), The trade wind field over the Pacific Ocean, *J. Appl. Meteorol.*, *15*, 698–704, doi:10.1175/1520-0450(1976)015<0698:TTWFOT>2.0.CO;2.

Zappa, C. J., A. T. Jessup, and H. H. Yeh (1998), Skin layer recovery of free-surface wakes: Relationship to surface renewal and dependence on heat flux and background turbulence, *J. Geophys. Res.*, *103*(C10), 21,711–21,722, doi:10.1029/98JC01942.

Zappa, C. J., W. E. Asher, A. T. Jessup, J. Klinke, and S. R. Long (2004), Microbreaking and the enhancement of air-water transfer velocity, *J. Geophys. Res.*, *109*, C08S16, doi:10.1029/2003JC001897.

Zappa, C. J., M. L. Banner, H. Schultz, A. Corrada-Emmanuel, L. B. Wolff, and J. Yalcin (2008), Retrieval of short ocean wave slope using polarimetric imaging, *Meas. Sci. Technol.*, *19*, 055503, doi:10.1088/0957-0233/19/5/055503.

Zhang, F., W. M. Drennan, B. K. Haus, and H. C. Graber (2009), On wind-wave-current interaction during the Shoaling Waves Experiment, *J. Geophys. Res.*, *114*, C01018, doi:10.1029/2008JC004998.

M. L. Banner, School of Applied Mathematics, University of New South Wales, Sydney, NSW 2052, Australia.

T. Dickey, Department of Geography, Graduate Program in Marine Sciences, University of California, Santa Barbara, Ellison Hall 1629, Santa Barbara, CA 93106, USA.

J. R. Gemmrich, Physics and Astronomy, University of Victoria, Victoria, BC V8W 3P6, Canada.

D. A. LeBel and C. J. Zappa, Ocean and Climate Physics Division, Lamont-Doherty Earth Observatory, Columbia University, 61 Rt. 9W, Palisades, NY 10964, USA. (zappa@ldeo.columbia.edu)

R. P. Morison, School of Mathematics and Statistics, University of New South Wales, Sydney, NSW 2052, Australia.

H. Schultz, Department of Computer Science, University of Massachusetts, Amherst, MA 01003, USA.